XPS and Transport Studies of Oxide Barriers in Tunnel Magnetoresistance Junctions

Von der Fakultät für Mathematik, Informatik und Naturwissenschaften der Rheinisch-Westfälischen Technischen Hochschule Aachen zur Erlangung des akademischen Grades eines Doktors der Naturwissenschaften genehmigte Dissertation

vorgelegt von

M. Sc. Physics

Harish Kittur

aus Gadag, Indien

Berichter: Universitätsprofessor Dr. Gernot Güntherodt
Universitätsprofessor Dr. Ulrich Rüdiger

Tag der mündlichen Prüfung: 02.07.2004

Contents

1 Introduction

Once studied primarily for their effects on light, thin magnetic films are today being layered to make complex structures with unique magnetic properties. Devices based on these structures are revolutionizing electronic data storage

……………. P. Grünberg in Physics Today (May 2001)

Hitherto, conventional electronics has only been exploiting the charge of charged particles during their motion in solids and the spin has been totally ignored. However with the discovery of the Giant Magnetoresistance (GMR) effect in ferromagnet/metal multilayers [1.1, 1.2] there has been a renewed interest in using also the spin of charged particles. The idea of taking into account and using the spin of charged particles has motivated physicists to explore and study novel concepts and physical phenomena. These efforts have lead to the formation of new fields of study generally called magnetoelectronics and spintronics. Among the various interesting manifestations of the role of spin of electrons in electrical transport is the spin dependent tunneling resistance between two ferromagnetic layers separated by an insulating barrier. This phenomena is generally called tunnel magnetoresistance (TMR) or spin dependent tunneling (SDT) or junction magnetoresistance (JMR). In this work we are mostly interested in exploring the physics and the technology of fabricating such TMR junctions. Specifically we were interested in the UV light-assisted oxidation process of thin Al layers to be used as barriers in TMR junctions. Besides the motivation was to explore the use of high spin polarization materials like Fe(110) [1.3] in such TMR junctions in order to obtain high

*TMR*s. In the current chapter we introduce the phenomenon of TMR and its historical background. Next we discuss the technical aspects of the barrier production. In chapter 2 we discuss the theory of thin film oxidation as given by Cabrera and Mott. We also discuss the role of ultraviolet light on the oxidation of thin metal films. In the third chapter on electron tunneling we briefly discuss and present the various aspects of tunneling employed in this work. Of special interest are the Rowell criteria of tunneling and the Glazmann-Matveev model of tunneling via localized defect states in the barrier.

Sample preparation and methods of characterization are presented in Chapter 4. In the next chapter 5 the results and measurements obtained in the course of this work are presented. Finally in the last chapter a brief summary and outlook is given.

1.1 Tunneling Magnetoresistance

Tunnel magnetoresistance (TMR) is the change in the tunnel resistance with the change in the relative magnetizations of two ferromagnetic (FM) films separated by a thin insulating barrier layer. Fig. 1.1 shows a typical TMR measurement in which the tunnel conductance or resistance is plotted as a function of the applied magnetic field.

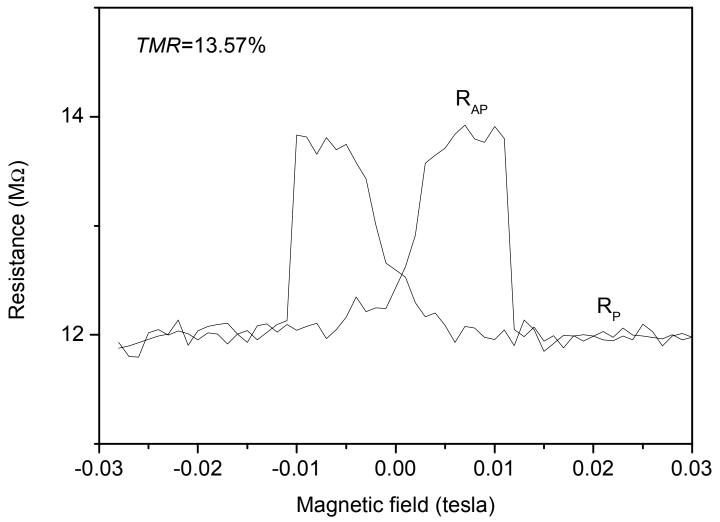

Fig. 1.1 A TMR curve of a Fe(110)/MgO(111)(4nm)/Fe(110) epitaxial tunnel junction deposited on a Mo(110)/ sapphire substrate.

The tunnel conductance is a maximum when the two ferromagnetic layer are magnetized parallel to each other and a minimum when the magnetizations of the two layers are anti-parallel to each other. In order to quantify the percentage change in the junction resistance one defines a tunnel magnetoresistance ratio *TMR* in terms of the junction resistances in the parallel and the anti-parallel magnetized state R_P and R_{AP} respectively where

$$TMR = \frac{\Delta R}{R_{AP}} \times 100 = \frac{R_{AP} - R_P}{R_{AP}} \times 100 \qquad 1.1$$

In order to achieve well resolved, stable parallel and anti-parallel magnetization states it is necessary that the two FM layers have different coercive or switching fields. Shown in

Fig. 1.2 is a typical magnetic hysteresis loop of a TMR sample, showing the different coercive fields of the two FM layers separated by an insulating barrier layer.

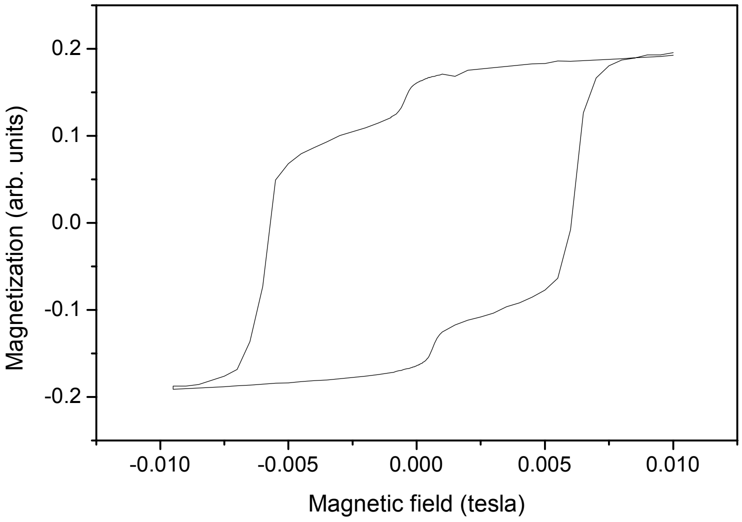

Fig. 1.2 The magnetic hysteresis loop of two FM layers separated by an insulating barrier layer measured in a SQUID magnetometer. The double hysteresis loop has its origin in the different coercive fields H_c of the two FM layers.

An array of FM/Insulator/FM tunnel junctions can be integrated with conventional Si based electronic technology to obtain the functionality of RAMs. Such RAMs based on TMR junctions are called magnetic RAMs (MRAMs) and have great potential applications because of the nonvolatility of the magnetizations of the two FM layers. Besides, the tunnel current does not change the relative magnetization of the two FM layers which means that the readout from such MRAMs is nondestructive. Such MRAMs are also expected to have very low read and write times of the order of 35 ns [1.4].

1.2 Historical background

In the year 1970 Tedrow and Meservey [1.5] first reported spin dependent tunneling. In their experiments by observing the electrons tunneling from Ni into superconducting Al separated by an insulating barrier, they could clearly demonstrate the effect of the spin polarization (SP) of the Ni electrons. Later in 1973 [1.6] by modifying the theory of superconducting–normal metal tunneling and defining a spin polarization

$$P = \frac{n\uparrow - n\downarrow}{n\uparrow + n\downarrow} = 2a - 1 \qquad 1.2$$

they measured the following P's; Fe, 44%; Co, 34%; Ni, 11%; and Gd, 4.3%.

Where $n\uparrow(\downarrow)$ is the density of electronic states at the Fermi level in the spin up (down) band, and

$$a = \frac{n\uparrow}{n\uparrow + n\downarrow} \qquad 1.3$$

is the fraction of the tunneling electrons whose magnetic moment is parallel to the applied magnetic field. Julliere in 1975 [1.7] then directly measured the conductance between Fe and Co films separated by an insulating barrier layer and obtained a TMR of 14%. Where

$$TMR = \frac{G_P - G_{AP}}{G_P} \times 100 = \frac{\Delta G}{G_P} \times 100 \qquad 1.4$$

G_P is the conductance in the parallel magnetized state and G_{AP} is the conductance in the anti-parallel magnetized state. Julliere employing Tedrow and Meservey's analysis assumed that in tunneling through the barriers the electron spins are conserved and the conductance is proportional to the product of the density of states. Fig 1.3 depicts graphically Julliere’s analysis. Shown in a) is the parallel magnetized state.

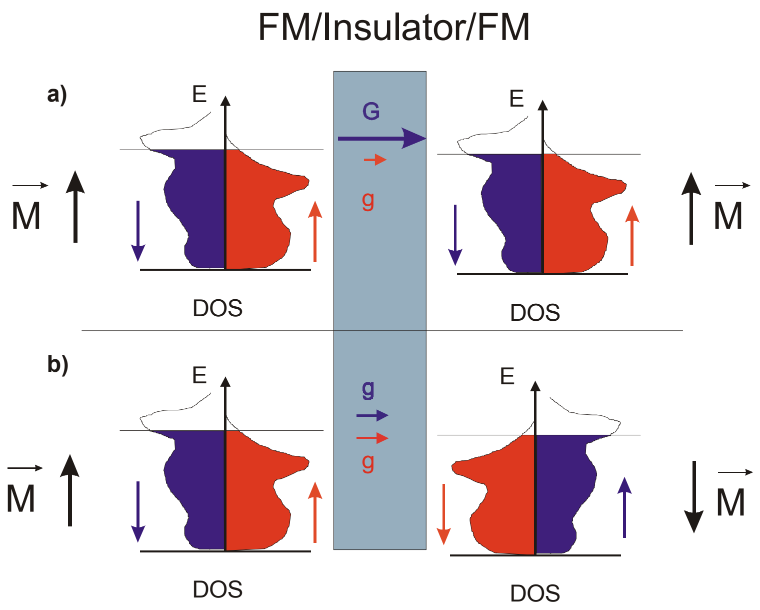

Fig. 1.3 Shown in a) is the schematic of the band diagrams in the case of the parallel magnetized state in which the tunnel conductivity **G**+g is high. Shown in b) is the anti-parallel magnetized state in which the tunnel conductivity is **g**+g is low.

The large number of spin down d band electrons near the Fermi level of the FM 1 (left) find a large number of empty unoccupied states in the spin down d band of the FM 2 (right), resulting in a larger tunnel conductance. In the anti-parallel magnetized state shown in Fig 1.3 b) in which the spin down d band electrons in FM 1 find fewer empty available states near the Fermi level in the spin down band, resulting in a comparatively lower tunnel conductivity.

$$G_P = a_1 a_2 + (1 - a_1)(1 - a_2) \tag{1.5}$$

and

$$G_{AP} = a_1(1-a_2) + a_2(1-a_1) \tag{1.6}$$

Which then gives us an expression for the *TMR* in terms of the spin polarizations P_1 and P_2 of the two FM layers called the Julliere formula:

$$TMR = \frac{2P_1P_2}{1+P_1P_2} \tag{1.7}$$

However, in spite of the challenges and the potential applications general widespread interest in the phenomenon remained latent except for a few exceptions [1.8, 1.9]. The discovery in the year 1988 of the phenomenon of GMR [1.1] and its potential applications as memory devices and read heads lead to a renewed interest in the phenomenon of TMR [1.10-16]. The interest in TMR was basically motivated by the possibility of the tunneling electrons conserving their spins in tunneling through the barrier layer to consequently give a high *TMR* and by the possibility of tuning the junction resistance by optimizing the barrier parameters like barrier height and barrier thickness, thus enabling the integration of such junctions with standard semiconductor technology.

Subsequently, Miyazaki et. al. [1.17] and Moodera et. al. [1.18] succeeded in measuring and reporting high *TMR*s at room temperature which were received with great interest by both the industrial and the scientific community.

1.3 Barrier production and oxidation

Even in the earliest stages of the discovery of the phenomenon of spin dependent tunneling it was known that the key to obtain pure tunneling conductance and high *TMR*s was the ability to produce good pinhole-free ultra-thin (~ 1-5 nm) homogeneous oxide barrier layers. A pinhole is a small opening in the barrier layer which could lead to metallic shorts between the top and the bottom electrode. The causes of the pinholes in the barrier layer could be one of the following.

1. Poor wetting of the barrier layer with the underlying electrode material leading to a Vollmer-Weber or island growth. i.e. when

$$\gamma_E < \gamma_{E/B} + \gamma_B \qquad 1.8$$

leading to a non zero ϕ, in order to satisfy the following equilibrium condition:

$$\gamma_E = \gamma_{E/B} + \gamma_B \cos\phi \qquad 1.9$$

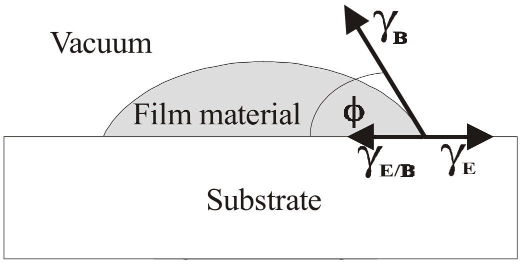

Fig 1.4 The equilibrium conditions of thin film growth.

where γ_E, γ_B, and $\gamma_{E/B}$ are the surface tension of the electrode/vacuum interface, barrier/vacuum interface and the electrode/barrier interface respectively.

2. Large sharp steps in the substrate and/or the lower electrode leading to effectively very thin barrier layers between the top and the bottom electrode in the vicinity of the step. It is therefore essential to have substrates and lower electrodes with roughness below 1 nm.

3. Presence of dirt particles on the substrate due to inadequate cleaning or the introduction of such dirt particles during the introduction of the substrate in the load-lock chamber.

After having chosen the proper materials and the deposition conditions it could usually be points no. 2 and 3 elucidated above that lead to the formation of pin-holes. To eliminate these it is therefore very essential to chose the right kind of substrate and ascertain its homogeneity and cleanliness.

Some of the various methods of producing the tunnel barriers are :

1. Depositing Al onto a liquid nitrogen cooled (77K) substrate followed by natural thermal oxidation at room temperature in pure oxygen or ambient air or air saturated with water vapour [1.6].
2. Employing a layer of semiconductor (Ge) and subsequently oxidizing it to form the insulating barrier layer [1.7].
3. Depositing Al at room temperature followed by natural thermal oxidation in air [1.17].
4. Al deposition onto a substrate cooled to 77K followed by oxygen plasma oxidation [1.18] at room temperature.

5. UV light-assisted oxidation [1.19, 1.20] in an oxygen and ozone atmosphere

Of the various materials tried out only aluminium oxide (Al_2O_3) has yielded the best and most reproducible results and is therefore the most popular. The aim of the work here undertaken was to try out UV light-assisted oxidation in an oxygen-ozone atmosphere.

1.4 Other required conditions in barrier production

Among the other conditions that the tunnel barrier should satisfy are the following:

1 The insulating barrier layer should be ultra-thin typically 0.7 to 2 nm. A thicker barrier could lead to an enhanced probability of possible spin flip tunneling processes leading to an effectively lower *TMR*. Besides it is known that the tunnel resistance increases exponentially with the barrier thickness [1.21, 1.23], therefore to keep the junction resistance low it is essential to keep the barrier thickness as low as possible(0.7-2 nm).

2 Rough interfaces lead to a dipolar coupling between the two FM layers commonly called Neel's orange peel coupling [1.24]. Such coupling reduces the *TMR* [1.25]. The interfaces of the barrier layers with the upper and lower FM electrodes should therefore be smooth so as to reduce between the two FM layers. to reduce the *TMR* value.

3 The barrier should be homogenous and should have a low defect density and impurity content so that the probability of defect mediated inelastic tunneling events which reduce the spin polarization of the tunneling electrons are reduced to a minimum.

4 If the barrier is produced by first depositing a metal film followed by oxidation then the oxidation process should not oxidize the underlying FM electrode. Under oxidation of the barrier layer also reduces the spin polarization of the tunnel electrons [1.26, 1.27].

5 The resistance of the junctions increases exponentially as the square root of the junction barrier height ϕ. It is therefore desirable to choose a material with a low barrier height. Aluminium oxide has a theoretical barrier height of 1 eV with reference to a Co film and is therefore well suited as a barrier layer.

6 The probability of having a defect or a short in the barrier increases with the increase in the junction area and it is therefore desirable to keep the junction area as small as possible.

2 Thin film oxidation

In this chapter we begin first by introducing the basic theoretical framework of thin film oxidation as elaborated by Mott [2.1, 2.2] and Cabrera and Mott [2.3]. Since our interest is mainly the low temperatue (room temperature) oxidation of very thin films of Al with thicknesses ranging from 1 to 2 nm we restrict ourselves to these ranges of thickness and temperature. Recent authors investigating the oxidation of thin Al films at room temperature also refer to the Cabrera Mott theory of thin film oxidation. The next sections then discuss the UV-light assisted oxidation of the Al films and the role played by the UV photoemission of electrons from the oxidizing Al film.

2.1 Oxidation of thin metal films

The oxidation of thin metal films is a very complex phenomenon which could involve many parallel processes participating simultaneously. An understanding of the oxidation of thin metal films is rendered difficult not only because of the complex and hard to resolve oxidation kinetics but also because of the strong dependence of the oxidation process on the chemical and physical nature of the metal films. Figure 2.1 taken from [2.4] shows schematically the various possibilities of early stage oxygen incorporation and the subsequent oxide formation. Stages 1, 2 and 3 involve the impingement of the O_2 gas molecules on the metal film surface, physisorption and the dissociation of the O_2 gas molecules. The initial oxidation of the metal film can then proceed in one or more of many simultaneous mechanisms as shown in stage 4.

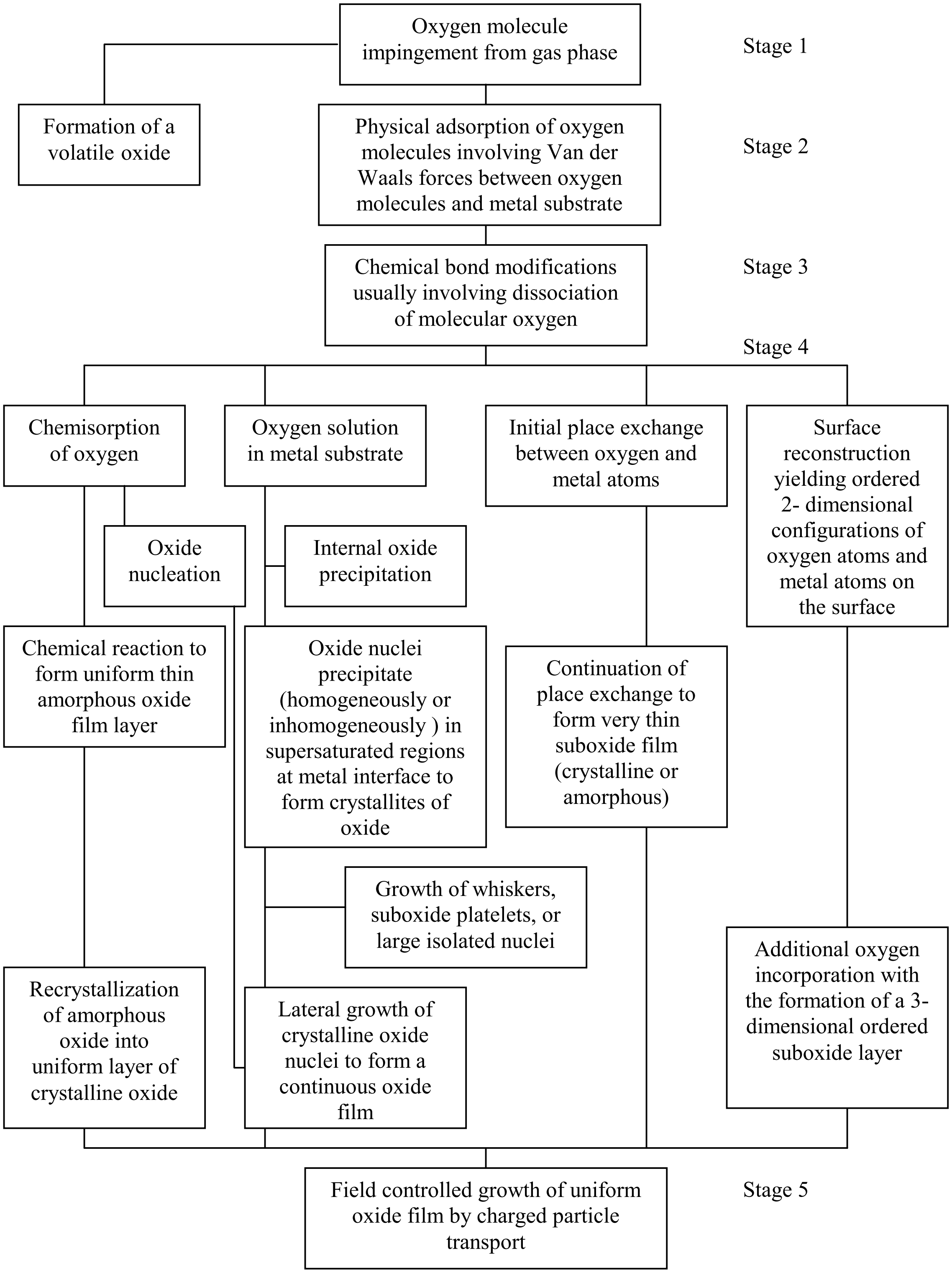

Fig. 2.1 Schematic of the various possibilities for early stage oxygen incorporation and subsequent oxide formation.

After the initial oxide formation the continued oxidation of the metal film may proceed via the field assisted diffusion of the charged particles. The field across the barrier has its origin in the contact potential difference of the metal film and the adsorbed O atoms on the surface of the oxide.

2.2 Cabrera-Mott theory of very thin film oxidation

Cabrera and Mott [2.3] first explained the oxidation of very thin metal films. It was observed that initially a very thin oxide film (about a monolayer thickness) is formed very rapidly and that after a few minutes or hours the oxidation slows down and then becomes negligibly small. Oxides of zinc and aluminium do not dissolve oxygen, they can, however, dissolve metal to become excess semiconductors. For such oxides one could assume a vanishing concentration of metal at the oxide/gas interface even for low pressures of O_2 and the oxidation rate would be independent of gas pressure. Oxides of copper and iron do dissolve oxygen to become defect semiconductors and a concentration gradient of oxygen is set up at the oxide-gas interface. The oxidation rate would thus depend on the oxygen pressure. However, Bardeen, Brattain and Shockley [2.5] proved it experimentally by the use of radioactive tracers that it is the metal species which diffuse and not the oxygen. Oxygen is taken up into the oxide by forming vacant cation sites, which diffuse away from the oxide-gas interface. Mott thus having realized the impossibility of the low temperature diffusion of O_2 in a closed Al film, proposed an alternative mechanism by which the oxidation could proceed.

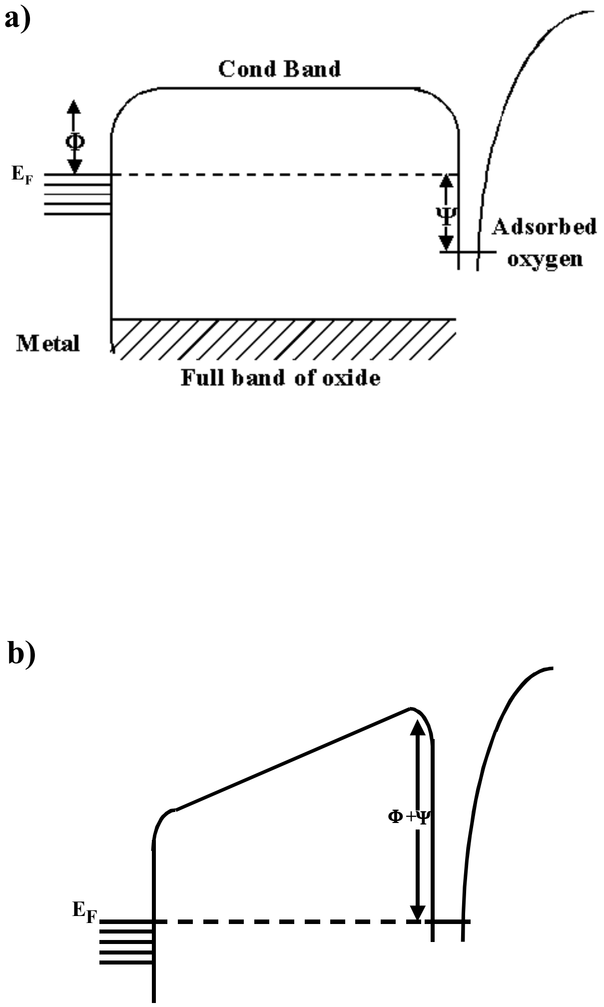

Fig 2.2 a) The schematic band levels are shown before equilibrium is reached, the lowest unoccupied level of adsorbed O_2 lies below the E_F of Al. In b) the band levels are shown after equilibrium is reached by the tunneling of the electrons from the metal/oxide interface to the adsorbed O atoms at the oxide/gas interface giving rise to O^- at the oxide/ gas interface.

He proposed the setting up of a strong electric field across the initial oxide layer due to the contact potential difference between the metal at the metal-oxide interface and the adsorbed O_2 at the oxide-gas interface (See Fig 2.2.). According to Mott it was this strong electric field that assisted the metal ions in moving through the oxide via interstitial sites and forming the oxide at the oxide-gas interface (See Fig 2.3).

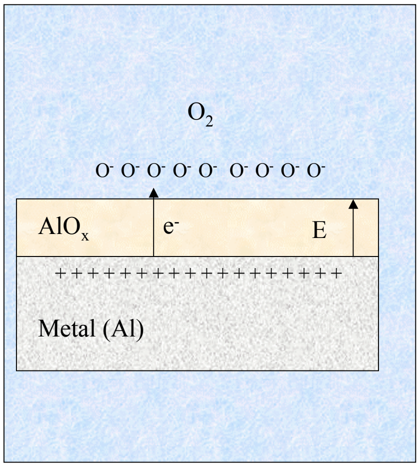

Fig 2.3 The initial rapid monolayer thickness oxide formation followed by the building up of the electric field E across the barrier due to the contact potential difference of the adsorbed O atoms and the electrons in the Al metal.

2.2.1 Basic theoretical approach of oxidation kinetics

The basic theoretical approach in evaluating the kinetics of the oxidation involves the calculation of the electrostatic potential in the oxide by means of Poisson's equation.

$$\frac{d^2V}{dx^2} = \frac{4\pi e}{\kappa}\left[n_i(x) - n_e(x)\right] \qquad 2.1$$

where κ is the dielectric constant of the growing oxide film and $n_i(x)$, $n_e(x)$ are the concentration of the interstitial ions and electrons in the oxide layer, respectively, and are obtained from Boltzmann's law

$$n_i(x) = n\exp(-eV/kT) \qquad 2.2$$

$$n_e(x) = n\exp(eV/kT) \qquad 2.3$$

where

$$n = \sqrt{(N_i N_e)}\exp\{-\frac{1}{2}(W_i + \phi)/kT\} \qquad 2.4$$

N_i is the number of interstitial positions per unit volume and $N_e = 2(2\pi mkT/h^2)^{3/2}$, m is the electron mass, k the Boltzmann constant and h the Planck constant. W_i is the heat of solution of a metallic ion in the oxide and ϕ is the energy required to remove an electron from the metal into the conduction band of the oxide. Therefore on substituting equations 2.2, 2.3 and 2.4 in equation 2.1 we get;

$$\frac{d^2V}{dx^2} = \frac{8\pi n}{\kappa}e\sinh(\frac{eV}{kT}) \qquad 2.5$$

On observing the form of equation 2.5 when x is large and V consequently small we get;

$$\frac{d^2V}{dx^2} = \frac{V}{X_0^2} \qquad 2.6$$

where

$$X_0 = \sqrt{\{\kappa kT/8\pi ne^2\}} \qquad 2.7$$

The solution of Eqn. 2.6 is $V = const. \exp(-x/X_0)$. It therefore is clear that the solution of the problem depends on the thickness x of the growing film. If $x >> X_0$, as in the case of oxidation of thick films, it may then be assumed that $n_e = n_i$. If $x << X_0$, as in the case of the oxidation of very thin or ultra-thin films then $n_e \neq n_i$ and there is no significant space charge set up. The motion of ions and electrons can then be considered independently. We are currently interested in this case. The current j due to any species is the sum of the diffusion current j_D and the current due to the electric field j_E.

$$j = j_D + j_E \tag{2.8}$$

j_D ,the diffusion current due to the concentration gradient of $n(x)$ is given by

$$j_D = -D\frac{\partial n(x)}{\partial x} \tag{2 .9}$$

where D is the diffusion coefficient of the species. j_E ,the current due to the field E in the oxide is given in terms of the mobility υ and the concentration n as

$$j_E = En\upsilon \tag{2 .10}$$

The ionic current j_i and the electronic current j_e from eqns. 2.8, 2.9 and 2.10 are then

$$j_i = -D_i\frac{\partial n_i}{\partial x} - En_i\upsilon_i \tag{2.11}$$

$$j_e = -D_e\frac{\partial n_e}{\partial x} + En_e\upsilon_e \tag{2.12}$$

On eliminating E from equations 2.11 and 2.12 in the steady state when both j_i and j_e are equal to j and making use of Einstein's equation

$$\frac{D}{\upsilon} = \frac{kT}{e}$$

we get;

$$j\{\frac{1}{n_e\upsilon} + \frac{1}{n_i\upsilon_i}\} = -\frac{kT}{e}\frac{\partial}{\partial x}\ln(n_e n_i) \tag{2.13}$$

The rate of change of the oxide thickness $dx(t)/dt$ is then obtained by assuming that the oxide thickness is proportional to the current j since every interstitial ion transfer to the oxide-gas interface forms oxide at the surface.

$$\frac{dx(t)}{dt} = Rj \qquad 2.14$$

where R is the constant of proportionality. Integrating equation 2.14 then gives the thickness of the oxide film $x(t)$.

2.2.2 Formation of very thin film

In the case of very thin films, the field is so strong that the drift velocity of the ions is not proportional to the field. In such cases Mott supposed that an ion has to go over a potential barrier U in order to move from one interstitial site to the next as shown in Fig. 2.4. P represents the position of a metal ion at the metal-oxide interface about to leave the metal. Q_1, Q_2…….. are interstitial positions in the oxide and S_1, S_2……. the tops of the potential barrier separating the interstitial points. The separation from P to S1, the top of the potential barrier is a' and the separation from S_1 to Q_1, S_2 to Q_2…… is denoted by a.

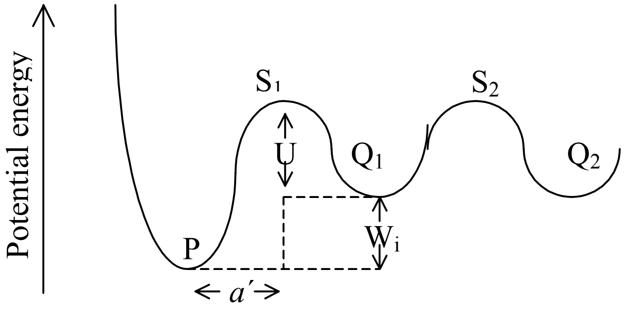

Fig. 2.4. Potential energy of an interstitial ion at the metal-oxide interface (P) and within the oxide (Q1,Q2).

Wi is the heat of solution of the metal ion in the oxide and U the activation energy for diffusion within the oxide.

In the absence of a field the rate at which an ion will move from one interstitial site to another is given by $\nu \exp(-U/kT)$, where U is the activation energy required to jump from one interstitial site to another. If q is the charge of the ion, the field will lower the barrier by $qaE/2$ for motion in the direction of the field, increasing the probability of movement to $\nu \exp\{-(U- qaE/2)/kT\}$. For motion against the field the probability of movement is reduced to $\nu \exp\{-(U+ qaE/2)/kT\}$. The drift velocity of interstitial ions is thus given by

$$u = va \exp(-U/kT)\{\exp(\frac{1}{2}qaE/kT) - \exp(-\frac{1}{2}qaE/kT)\} \qquad 2.15$$

For large values of the field one can neglect the negative exponent in equation 2.15. Thus

$$u \sim va \exp(-U/kT)\{\exp(\frac{1}{2}qaE/kT)\} \qquad 2.16$$

Thus when the field is strong the motion of the ions is preferentially in one direction and there is no local equilibrium between the metal and oxide. Every ion which escapes from the metal is pulled to the surface where it is oxidized. The rate of oxidation for such strong fields is determined only by the rate at which ions escape from the metal.

Therefore the rate at which the metal atoms will escape over the barrier to Q_1 in the presence of the field is given by $\nu \exp(-W/kT)\exp(qa'E/kT)$. The rate of growth of the film is thus given by

$$\frac{dx}{dt} = N'\Omega\nu \exp(-W/kT)\exp(\frac{qa'E}{kT}) \qquad 2.17$$

Where N′ is the number of ions per unit surface area in the metal interstitial sites. Ω is the volume of oxide per metal ion. Equation 2.17 can be expressed as

$$\frac{dx}{dt} = u \exp(\frac{X_1}{x}) \qquad 2.18$$

Where

$$X_1 = qa'V/kT \qquad 2.19$$

V is the contact potential difference between the metal and the adsorbed O atoms.

$$u = u_0 \exp\left(-\frac{W}{kT}\right) \text{ with } u_0 = N'\Omega\nu \qquad 2.20$$

X_1 is of the order of $10^{-6} - 10^{-5}$ cm. u_0 is lesser than 10^4 cm/sec. It can be seen from Eqn. 2.18 that for $x << X_1$ the rate of growth is rate of growth of the oxide film is very large and under specific circumstances there is a certain limiting thickness X_L of the oxide film. This can be seen by assuming that the oxide growth is negligible when one monolayer of oxide is added in 10^5 sec so that dx/dt = 10^{-13} cm/sec. One then obtains from Eqns. 2.18, 2.19 and 2.20

$$X_L = \frac{qa'V}{W - 39kT} \qquad 2.21$$

Thus, there exists a critical temperature $W/39k$ below which the film grows rapidly up to some critical thickness X_L.

For $x << X_1$ on integrating Eqn. 2.18 by parts and neglecting the higher order terms in x/X_1 one gets an inverse logarithmic law of growth.

$$-\frac{X_1}{x} = \ln\left(\frac{X_1 ut}{X_L^2}\right) \qquad 2.22$$

The above equation can be simplified as

$$\frac{X_1}{x} = A - \ln t \qquad 2.23$$

where A is a constant and t the oxidation time.

2.3 UV-light assisted oxidation

It is well known that UV light can dissociate molecular oxygen to form O and O_3. O_2 has a bond dissociation energy of 5.1 eV (λ=240 nm) and the following reactions take place for UV light with λ < 240 nm [2.6, 2.7]

$$\begin{gathered} O_2 + h\upsilon \rightarrow 2O \\ J_1 = 1.6 \times 10^{-20} cm^2 (\lambda = 185nm) \end{gathered} \qquad 2.24$$

$$\begin{gathered} O + O_2 + M \rightarrow O_3 + M \\ k_2 = 2.8 \times 10^{-12} cm^3 molecule^{-1} s^{-1} \end{gathered} \qquad 2\ .25$$

$$\begin{gathered} O_3 + O \rightarrow 2O_2 \\ k_3 = 2.8 \times 10^{-15} cm^3 molecule^{-1} s^{-1} \end{gathered} \qquad 2.26$$

$$\begin{gathered} O_3 + O_2 \rightarrow O_2 + O_2 + O \\ k_4 = 7.7 \times 10^{-16} cm^3 molecule^{-1} s^{-1} \end{gathered} \qquad 2.27$$

Where J_1, k_2, k_3 and k_4 are the rate constants. M in equation 2.21 is a third body. O and O_3 are highly reactive and could thus lead to the quicker formation of a thicker initial oxide layer. The enhancement of the oxidation process has indeed been confirmed experimentally [2.8]. The UV light-assisted oxidation of thin metal films thus enhances the rate and the final limiting thickness X_L of the oxide film formed. Besides the highly reactive species available Cabrera and Mott noted that the photoemission of electrons from the metal film due to the incident UV light could also enhance the oxidation rate and the final limiting thickness X_L of the oxide film formed. Under the influence of UV light the electronic equilibrium represented in Fig 2.2 b) is disturbed due to the additional flux of electrons coming from the metal into the metal oxide. In order to reestablish the electronic equilibrium the adsorbed O levels are raised by an amount ξ as shown in Fig. 2.5 The field in the oxide is thus raised by an amount ξ so that the number of electrons tunneling back to the metal is also increased and local electronic equilibrium is established. The increased field set up in the oxide due to the photoemission of electrons increases the rate (Eqn. 2.17) at which metal ions from the metal-oxide interface arrive at the surface where they are oxidized. The higher field set up also increases the limiting thickness (Eqn 2.21) of the oxide film formed.

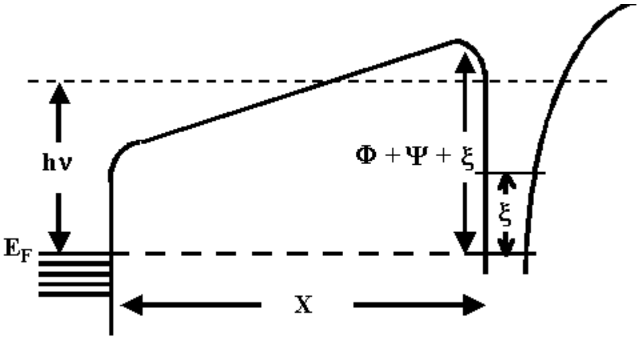

Noting that the value of ξ will depend on the thickness x of the oxide layer Cabrera has made the following qualitative analysis. For x → 0, ξ → 0 because for small values of x electrons can pass very easily in both the directions through the oxide and the equilibrium shown in Fig. 2.2 b) is maintained. For higher values of x the transmission coefficient of electrons through the oxide rapidly decreases and in order to obtain a new equilibrium ξ becomes nonzero. Thus ξ increases with x and its maximum value is hν. Assuming that the mean free path of the electrons in the oxide is larger than the thickness, Cabrera [2.9] has obtained the following relation for ξ as a function of x.

$$\frac{3}{2}\frac{\psi+\xi}{\phi+\psi}\frac{x_0}{x}=1-(1-\frac{h\nu-\xi}{\phi+\psi})^{3/2} \qquad 2.28$$

where

$$x_0 \sim \frac{1}{(\phi+\psi)^{1/2}} \qquad 2.29$$

The maximum value of ξ obtained from Eqn. 2.28 is $h\nu$ which is consistent with the fact that ξ can't be greater than $h\nu$. For small values of $h\nu - \xi$ one obtains from Eqn. 2.28

$$\frac{\xi}{h\nu} = 1 - \frac{\psi + h\nu}{h\nu}\frac{x_0}{x + x_0} \qquad 2.30$$

The field E across the oxide is now given by

$$E = \frac{\psi + \xi}{ex} \qquad 2.31$$

For values of x larger than $x_0\psi/h\nu$ we get from Eqn. 2.30

$$E = \frac{\psi + \xi}{e(x + x_0)} \qquad 2.32$$

On substituting Eqn. 2.32 in Eqn. 2.18 and again solving for the limiting thickness X_L' we obtain

$$X_L' + x_0 = \frac{qa'(\psi + h\nu)}{W - 39kT} \qquad 2.33$$

On dividing Eqn. 2.33 by Eqn. 2.21 and replacing the contact potential difference V by ψ we get

$$\frac{X_L' + x_0}{X_L} = \frac{\psi + h\nu}{\psi} \qquad 2.34$$

E will be ψ/ex for values of x smaller than $x_0\psi/h\nu$ and the UV light will have no influence on the oxidation rate and X_L.

3 Electron tunneling

In this chapter we introduce some of the basic tunneling concepts and criteria used extensively in this work. We begin with the Simmons model of tunneling between two metallic films separated by an insulating barrier. Since the results of I-V curve fits to the Brinkman, Dynes, and Rowell (BDR) theory of tunneling between metal films separated by an asymmetrical barrier did not yield very convincing results the BDR theory is discussed only briefly. In the following section the four Rowell criteria of detecting tunneling between metal films are elaborated. Finally we discuss the Glazmann-Matveev (GM) model of inelastic tunneling via chains of localized defect states. The GM model is used extensively in this work to interpret the results and measurements of tunnel junctions with AlOx and MgO barriers.

3.1 Simmons model

Sommerfeld and Bethe [3.1] were the first to make a theoretical study of the phenomena of tunneling between two metal electrodes separated by an ideal thin insulating barrier for the case of very low voltages and high voltages. Holm [3.2] extended the theory to include intermediate voltages. Both the theories were derived independently using the Wentzel, Kramers and Brillouin (WKB) approximation. In the WKB approximation the probability $D(E_x)$ that an electron penetrates a potential barrier of height $V(x)$ is given by

$$D(E_x) = \exp\{-\frac{4\pi}{h}\int\left[2m(V(x)-E_x)\right]^{\frac{1}{2}} dx\} \qquad 3.1$$

Simmons [3.3] first derived a single theory for the current flow through a generalized barrier and for all voltages using the WKB approximation. For a rectangular barrier of height φ_0 and thickness s he obtained the following expressions for the current voltage relationship for different bias voltage ranges.

Low-Voltage Range: $V \sim 0$

$$J = 3.16\times 10^{10}\,\varphi_0^{\frac{1}{2}}(V/s)\exp(-1.025 s\varphi_0^{\frac{1}{2}}) \tag{3.2}$$

Intermediate Voltage Range: $0 < V < \varphi_0$

$$J = \frac{6.2\times 10^{10}}{s^2}\{(\varphi_0 - \frac{V}{2})\exp\left[-1.025 s(\varphi_0 - \frac{V}{2})^{\frac{1}{2}}\right] - (\varphi_0 + \frac{V}{2})\exp\left[-1.025 s(\varphi_0 + \frac{V}{2})^{\frac{1}{2}}\right]\} \tag{3.3}$$

High Voltage Range: $V > \varphi_0$

$$J = 3.38\times 10^{10}(\frac{V^2}{s^2\varphi_0})\{\exp(-0.689\frac{s\varphi_0^{\frac{3}{2}}}{V}) - (1+\frac{2V}{\varphi_0})\exp(-0.689\frac{s\varphi_0^{\frac{3}{2}}}{V})(1+\frac{2V}{\varphi_0})^{\frac{1}{2}}\} \tag{3.4}$$

Where J is the current density expressed in Acm^{-2}, the height of the barrier φ_0 is in volts and s, the thickness of the barrier is in Å units. Equation 3.3 was used extensively in this work to fit the I-V characteristics of the tunnel junctions and to obtain the barrier height and width.

3.1.1 Temperature dependence in Simmons model

Simmons [3.4] also obtained the temperature dependence of the tunnel current in the WKB approximation and got the following relation for intermediate voltages $V \leq \varphi_0$

$$J(V,T) = J(V,0)\left\{1+\left[3\times10^{-9}\times\frac{s^2T^2}{(\varphi_0-\frac{V}{2})}\right]\right\} \qquad 3.5a$$

The above equation 3.5 a can be simplified and the temperature dependence of the conductance *C(T)* can be expressed as

$$C(T) = a + bT^2 \qquad 3.5b$$

where a and b are constants. The temperature dependence of the tunnel conductivity of many junctions was fitted with Eqn. 3.5b. The fits though good were found to be not perfect. Besides, Simmons model is valid only for ideal tunnel barriers and does not take into account the realistic tunneling barriers with defect states within them. Thus Eqns. 3.5a and 3.5b are inadequate to describe the temperature dependence of the tunnel conductivity.

3.2 Brinkman, Dynes and Rowell theory

Brinkman, Dynes and Rowell [3.5] calculated the tunneling conductance of asymmetrical barriers in the WKB approximation and obtained the following relation for the tunneling conductance as a function of the bias voltage.

$$\frac{G(V)}{G(0)} = 1-\left(\frac{A_0\Delta\varphi}{16\bar{\varphi}^{\frac{3}{2}}}\right)eV+\left(\frac{9}{128}\frac{A_0^2}{\bar{\varphi}}\right)(eV)^2 \qquad 3.6$$

Where $\Delta\varphi = \varphi_2 - \varphi_1$ is the asymmetry of the barrier, $\bar{\varphi} = (\varphi_1 + \varphi_2)/2$, $A_0 = 4(2m)^{1/2}d/3h$ and $G(0) = (3.16 \text{ x } 10^{10}\bar{\varphi}^{1/2}/d)\exp(-1.025\, d\bar{\varphi}^{1/2})$

Where *d* is the barrier thickness and *h* is the Plank's constant. They also proved that the conductance minimum of asymmetrical barriers is not at zero bias but shifted by an amount V_{min} where

$$eV_{\min} = 0.649\left(\frac{\Delta\varphi}{d\,\varphi^{-\frac{1}{2}}}\right) \qquad 3.7$$

3.3 Rowell criteria of tunneling

In order to quickly detect and judge tunneling behavior in tunnel junctions Giaever and Rowell formulated a set of criteria, which are now popularly called as the Rowell criteria for tunneling [3.6]. The Rowell criteria for tunneling are as follows:

1. Junction resistances are inversely proportional to the junction area.
2. An exponential dependence of the junction resistance on the tunnel barrier thickness.
3. An increase in the junction resistance with decreasing temperature.
4. Existence of non-linear I vs. V curves.
5. The existence of a clear superconducting gap below T_c in the I-V characteristic if a superconductor replaces one of the junction electrodes.

Recently investigations have shown that even junctions with pin-holes can exhibit a nonlinear I-V characteristic [3.7]. The mere observation of a nonlinear I-V characteristic could mislead one to the conclusion that the junction exhibits tunneling. It is also possible that junctions with pin-holes can mimic the exponential dependence of the junction resistance on the barrier thickness [3.8]. Thus in the light of these most recent observations it is clear that the most reliable criteria of establishing tunneling in junctions are Rowell's criteria number 3 and 5 mentioned above.

3.4 Potential barriers incorporating localized defect states.

Many authors in the past have realized the inadequacy of the assumption that the potential barrier in tunnel junctions can be replaced by a uniform potential barrier ϕ which does not exhibit any intrinsic properties, e.g., defects. Most tunneling barriers contain defects and deviate from an ideal insulating barrier. J. Halbritter [3.9] has summarized the various anomalies detected in tunnel junctions and attributed these to the intrinsic properties of the tunnel barriers. He has summarized [3.10, 3.11] that real tunnel barriers have several tunnel channels and any realistic description of tunneling should include at least the following three channels connected in parallel [3.9]:

1. The channel corresponding to $\bar{\phi}$, the commonly assumed high potential barrier of the insulating (or semiconducting) barrier layer.
2. The narrow low lying channels $\bar{\phi}^*$ corresponding to the lower potential barriers connecting the two electrodes.
3. The channels due to the localized states near the Fermi level yielding a rise in the tunnel current due to resonant tunneling.

In his potential barrier model incorporating localized states to explain tunnel anomalies he has shown that the localized states at E_F and the dynamics are most important for tunneling through real tunnel barriers. The localized states hybridize with conduction electron status to form interface states that can yield a strong coupling to surface plasmons, phonons and spins. These states cause diffuse surface scattering and enhance the tunneling current due to resonant tunneling. The enhanced interaction of the localized electrons with surface plasmons, phonons and spins yield strong *V*, *T* and time dependencies in the tunnel current which produce zero bias anomalies, inelastic processes, noise and barrier reduction with increase in temperature.

3.4.1 Glazman-Matveev model of inelastic tunneling

Glazman and Matveev [3.12] proposed a microscopic model of resonant tunneling via chains of localized defect states which offers a convenient and useful tool in analyzing the temperature and bias dependence of the tunnel conductivity [3.13-15]. A chain of localized defect state is a conductance channel with different number of localized defect states. A chain of n = 0 corresponds to a channel with no defect states and a chain of n = 1 corresponds to a conductance channel via one localized defect state and so on for higher values of n. In their model which includes the electron-phonon coupling the authors find that the *T* and *V* dependence of the tunnel conductance in different *T* and *V* ranges is canonical and obeys the form

$$G_n(V) = a_n \cdot V^{\left(n-\frac{2}{n+1}\right)}, \text{ for } k_B T << eV \qquad 3.8$$

$$G_n(T) = b_n \cdot T^{\left(n-\frac{2}{n+1}\right)}, \text{ for } eV << k_B T \qquad 3.9$$

and the total conductance *G(V,T)* is given by;

$$G(V,T) = G_0 + \sum_{n=1}^{\infty} G_n(V,T) \qquad 3.10$$

Where G_0 represents the conductance due to direct elastic tunneling and G_n represents the conductivity due to resonant tunneling via a chain of n localized defect states for n ≥ 1. Fig. 3.1 depicts schematically the various channels of resonant tunneling via localized defect states.

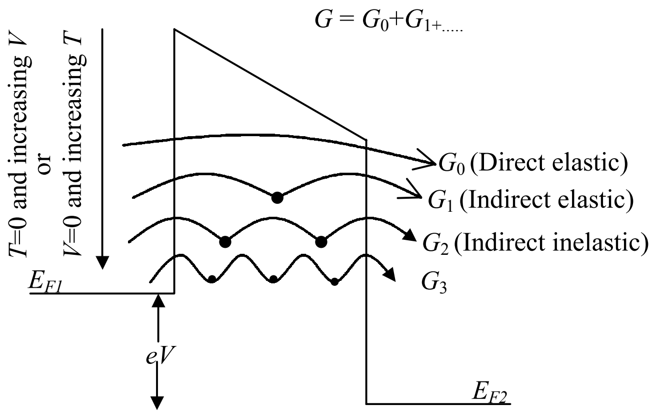

Fig. 3.1. The various channels dominating the tunnel conductance in the Glazman-Matveev model.

At T = 0 and V = 0, the conduction is predominantly due to direct elastic tunneling corresponding to the term G_0 in equation 3.10. At T = 0 K on increasing V, more and more resonant tunnel channels open up and dominate the conductivity beginning from the n = 1 indirect elastic term and later on switching over to the n = 2 indirect inelastic terms and so on. At V = 0, the temperature dependence of the conductivity is similar to the bias voltage dependence of the tunnel conductivity leading to the opening up and dominance of the conductivity due to the resonant tunneling via higher-n chains of localized defect states with increasing temperature.

3.5 Separating the elastic and inelastic component of the tunnel conductance

Some authors have found it convenient and useful to separate the elastic and inelastic component of the tunnel conductance of TMR junctions [3.14, 3.15]. Especially used in this work is the method of Höfener et. al. [3.15] which assumes that the n = 0 and n = 1 elastic tunneling terms conserve the spin polarization of the tunneling electrons and n ≥ 2 inelastic terms destroy the spin polarization and are magnetic field independent.

Hence $G = G^E + G^I$

where the superscripts E and I correspond to the elastic and inelastic component. Then $TMR_{measured}$ is given in terms of the change in conductance ΔG and the conductance in the anti-parallel state G_{AP} by the equation

$$TMR_{measured} = \left(\frac{\Delta G}{G_{AP}}\right)_{measured} = \frac{\Delta G^E}{G^E_{AP} + G^I_{AP}} \qquad 3.11$$

On dividing both sides of Eqn. 3.11 by G^E_{AP} and rearranging the terms we get;

$$TMR_{Julliere} = \left(\frac{\Delta G}{G^E_{AP}}\right)_{Julliere} = \left(1 + \frac{G^I_{AP}}{G^E_{AP}}\right)\left(\frac{\Delta G}{G_{AP}}\right)_{measured} \qquad 3.12$$

Thus, if one is able to evaluate the ratio

$$\rho = \frac{G^I_{AP}}{G^E_{AP}} \qquad 3.13$$

then it is possible to compare measured the *TMR* with the *TMR* obtained from Julliere's model in which all the spin polarization is conserved.

$$TMR_{observed} = \left(\frac{1}{1+\rho}\right) TMR_{Julliere} \qquad 3.14$$

By fitting the temperature dependence of the tunnel conductance and obtaining the constants G_0, G_1, G_2.....it is possible to obtain the temperature dependence of the *TMR* where

$$\rho = \frac{G_2 T^{\frac{4}{3}} + G_3 T^{\frac{5}{2}} + G_4 T^{\frac{18}{5}} + \dots\dots\dots}{G_0 + G_1} \qquad 3.15$$

Similarly by fitting the bias dependence of the tunnel conductance and obtaining the constants G_0, G_1, G_2, G_3, …from the fits, it is possible to obtain the bias dependence of the *TMR* where

$$\rho = \frac{G_2 V^{\frac{4}{3}} + G_3 V^{\frac{5}{2}} + G_4 V^{\frac{18}{5}} + \dots\dots\dots}{G_0 + G_1} \qquad 3.16$$

4 Sample preparation and Methods of characterization

In this chapter we begin by introducing UV light-assisted oxidation of ultra-thin Al layers and the different geometries in which UV light-assisted oxidation can be carried out, i.e. the direct and the indirect UV light-assisted oxidation. We then briefly introduce and explain the sample deposition and preparation techniques and the different means of defining the tunnel junctions. The concluding sections are the sample characterization techniques like XPS and electrical transport measurements in a liquid Helium cooled cryostat equipped with a superconducting magnet.

4.1 UV light-assisted oxidation

As mentioned previously in the first chapter the main aim of this work was to study the UV light assisted oxidation of ultra-thin Al layers to form the oxide barrier layer. It has already been mentioned in section 2.3 that O_2 on being irradiated with UV light produces, by the photodissociation of O_2, ozone and atomic O, both of which are highly reactive [4.1]

$$O_2 \overset{UV}{\rightleftharpoons} O + O_3 \qquad 4.1$$

It could therefore be an advantage over natural thermal oxidation in air or O_2 where the oxidation time, typically 12-24 hrs. [4.2], is very large. Secondly, because of the intermediate and controllable UV light-assisted oxidation times it could be possible to tune the resistance area (R×A) products of TMR junctions. UV light-assisted oxidation could thus also fill the gap in the oxidation times, between the very short oxidation times in plasma oxidation and the very long oxidation times for natural thermal oxidation [4.3]

Thirdly, UV light-assisted oxidation can have an advantage over the exceedingly rapid plasma oxidation process, in which energetic ions are made incident on the metal film. These energetic ions could introduce a high defect density in the film. As discussed in chapter 3 an increase in the defect density could lead to an increase in the tunneling via defect states. The UV light assisted oxidation process can be carried out in two geometries, direct and indirect UV light-assisted oxidation.

4.1.1. Indirect UV light-assisted oxidation

In this method the UV light does not shine directly onto the metal film but only photo-dissociates O_2 to form O_3 and O. The oxidation proceeds only due to the chemical action of O, O_2 and O_3 on the metal film. Fig. 4.1 shows schematically the indirect UV light-assisted oxidation geometry. The UV light only acts on the inlet O_2 gas to form a mixture of O, O_2 and O_3 in the oxidation chamber.

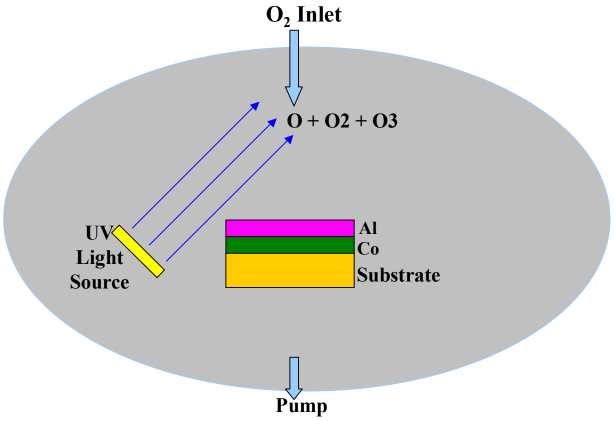

Fig. 4.1. The indirect UV light-assisted oxidation of an Al film

Most of the samples prepared by indirect UV light assisted oxidation were prepared with a low power 15 W in-situ UV light source, unless specified otherwise and with a gas flow F_G = 0 l/min i.e. no gas flow during oxidation. The O_2 gas was let into the oxidation chamber under vacuum till the desired gas pressure was reached and then the valves of both the O_2 inlet and the membrane pump were closed.

4.1.2. Direct UV light assisted oxidation.

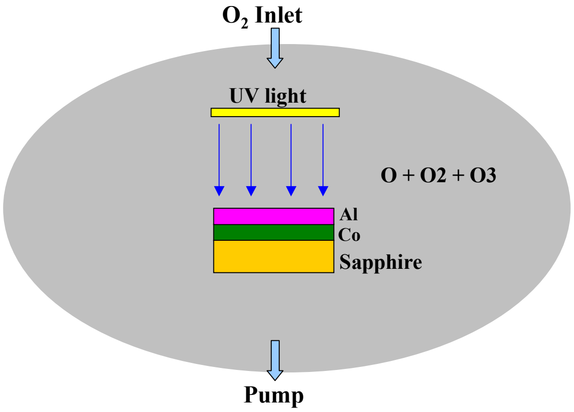

Fig. 4.2. The direct UV light assisted oxidation of an Al film

In this case the UV light is made to shine directly onto the metal film surface to produce photoemitted electrons from the metal film. The oxidation in this case, therefore, proceeds not only by the action of O, O_2 and O_3 but also due to the photoelectric enhancement of the oxidation process. This mechanism has already been dealt with in greater detail in Chapter 2.

4.2 Sample preparation

The samples were made by depositing the thin films in a UHV MBE chamber and the oxidation of the Al layer was carried out in the load lock chamber (oxidation chamber) equipped with a UV light source and a feed back loop to precisely control the gas pressure in the load lock chamber. Fig. 4.6 shows a schematic diagram of the oxidation chamber. The pressure in the load chamber was monitored by a Baratron and the gas inlet was through a solenoid valve.

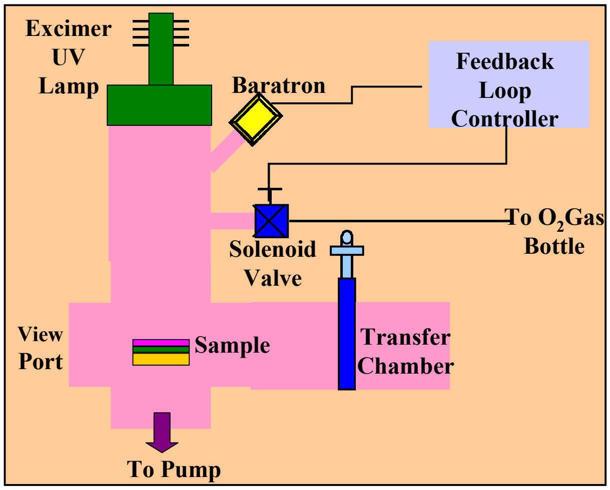

Fig 4.6 A schematic diagram of the load-lock/oxidation chamber equipped with a UV Excimer lamp source and a feed-back controlled mechanism to precisely control the absolute gas pressure in the chamber.

The pressure monitored by the Baratron is fed to a feedback loop controller which in turn then sets the current in the solenoid valve to achieve the desired pressure in the load lock chamber. A simple gas flow indicator monitored the gas flow rate into the oxidation chamber.

4.3 Shadow Mask Deposition

In the initial stages of the study the junctions were defined by a shadow mask deposition technique as shown in Fig. 4.7.

The masks made out of Mo foils were designed in the institute and fabricated in the institute workshop. The lower FM Co layer was first deposited using mask 1, the mask was then changed to mask 2 which deposits a rectangular Al film parallel to the Co film deposited by mask 1. The Al film is then oxidized in the load lock chamber according to the desired oxidation parameters. The load lock chamber is then pumped down to UHV and the sample transferred to the MBE chamber. Now with the help of mask 3 the cross strips of the Co FM layer are deposited to form 3 junctions of area $150 \times 150\ \mu m^{2.}$

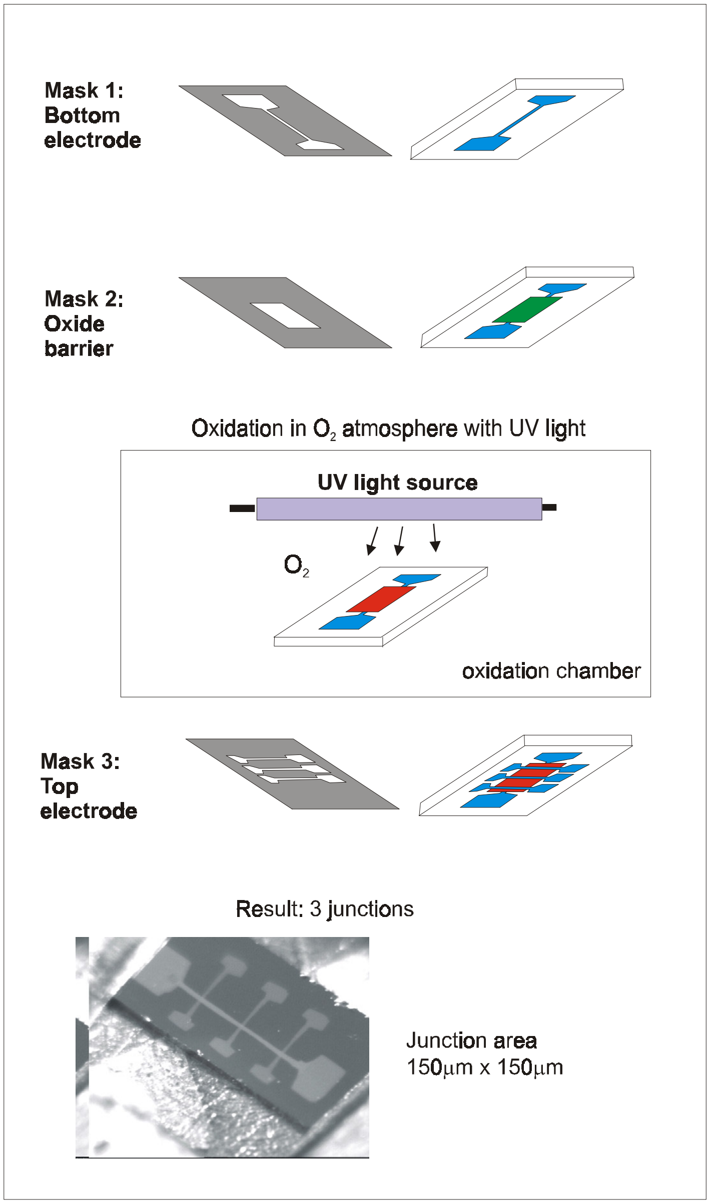

Fig 4.7 Shadow mask deposition of the individual layers to form junctions in the cross geometry

4.4 Microstructured Junctions

In the later stages of the study the tunnel junctions were defined by microstructuring the MBE deposited multilayers with the help of UV and e-beam lithography and Ar ion etching. The FM/ Insulator/ FM multilayers are first deposited and prepared in the MBE chamber without any masks. The multilayer were then microstructured to define junctions of area 25 μm^2, 100 μm^2 and 400 μm^2 and the contact pads for the upper and lower FM electrodes. Fig 4.8 shows schematically the various steps involved in micro-structuring the multilayers to obtain TMR junctions. The whole process can be for convenience of description divided into four major parts consisting of the following:

1. Defining the bottom electrode

   A negative photoresist (AR-U 4040) is first spun onto the multilayer. The bottom electrode is then defined by exposing the negative photoresist to UV light through a mask. The photoresist is then developed followed by an Ar ion beam etching to obtain a stripe of the multilayer of width 150μm.

2. Defining the tunnel area

   The photo-resist from the previous process step is removed and a negative electron-beam resist (AR-N-7500.18) is spun onto the sample. The junction area is then defined by e-beam lithography according to the desired junction area, typically 20 x 20, 10 x 10 or 5 x 5 μm^2. The photoresist is then developed followed by an Ar ion etching process step. The Ar ion etching is carried out in such a manner that the etching proceeds beyond the insulating layer separating the two FM layers but much before the end of the lower FM electrode. This is done so as to well separate the two FM layers and to obtain a large area lower FM electrode.

3. Depositing the SiO_2 insulating layer to separate the top and bottom contact electrodes

   A 45 – 60 nm thick SiO_2 layer is then sputtered onto the sample followed by a lift-off in acetone. The next process step employs a positive photoresist for UV lithography to define the top Au contact electrode.

4. Depositing the top Au contact electrode

   The top Au contact layer is sputtered followed by a lift-off process step in acetone to obtain the top Au contact electrode.

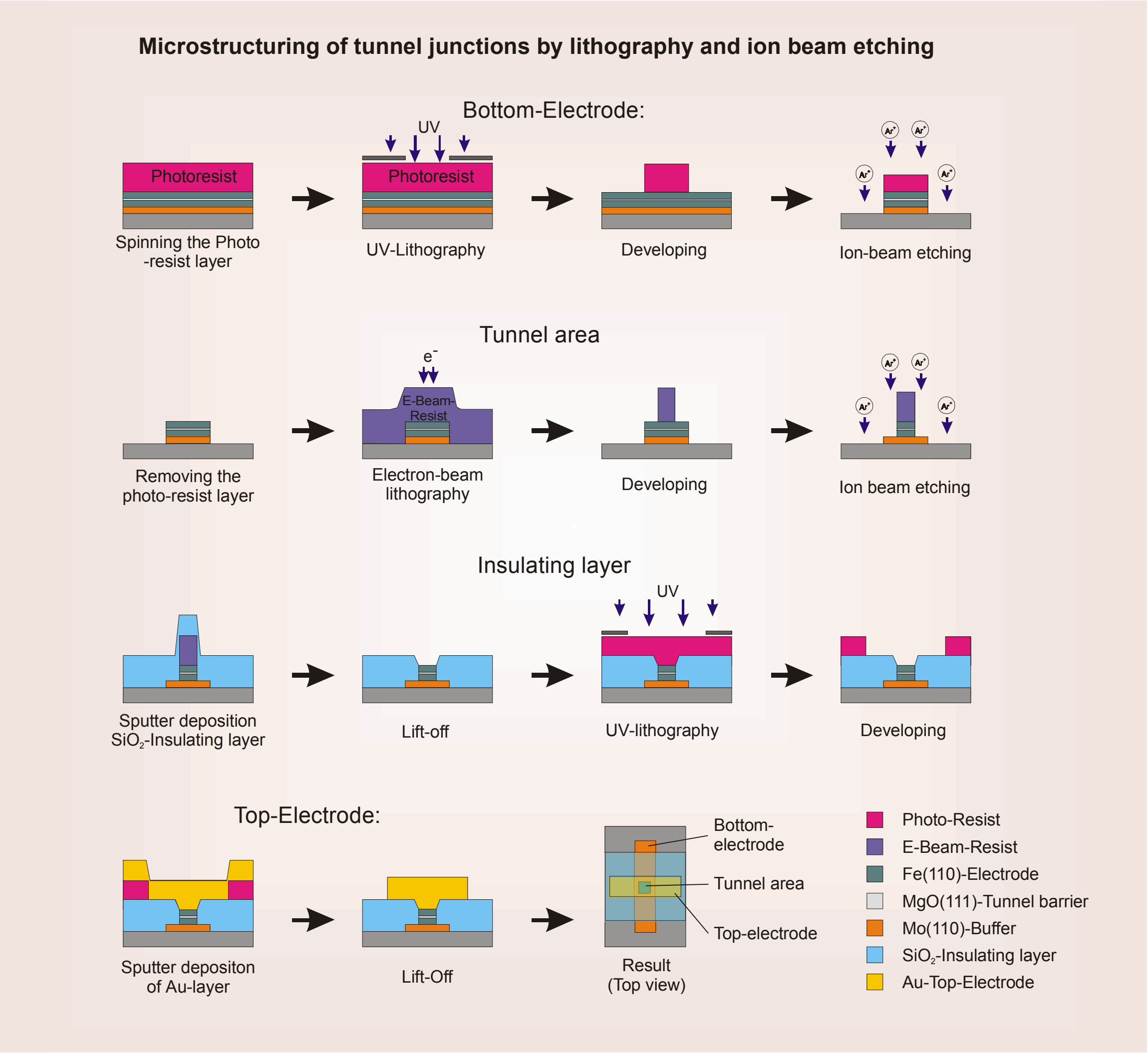

Fig 4.8 The steps involved in microsructuring the FM/ Insulator/ FM multilayers

4.5 Methods of Characterization

4.5.1 Transport measurements

The transport measurements of the TMR junctions were made in a liquid He cooled cryostat equipped with a superconducting magnet. It was possible to measure the tunnel conductivity or resistivity as a function of the applied bias voltage, the temperature and the magnetic field applied in the plane of the sample. All measurements were made in the four- point probe geometry to avoid measuring the contact and lead resistances. In the liquid He cooled cryostat it was possible to make measurements in the temperature interval 4.2 – 300K. Shown in Fig 4.9 is a schematic diagram of the liquid He cooled cryostat. In the middle of the cryostat is the sample room for the introduction of the samples. The sample room is separated from the liquid He tank by vacuum and it is possible to transfer liquid He from the tank into the sample room by opening a needle valve at the top end and pumping into the sample room. The liquid He tank is surrounded by radiation shielding material and vacuum and is further shielded by the liquid nitrogen tank shown in Fig. 4.9. It is possible to control the temperature of the sample by suitably cooling and heating the sample.

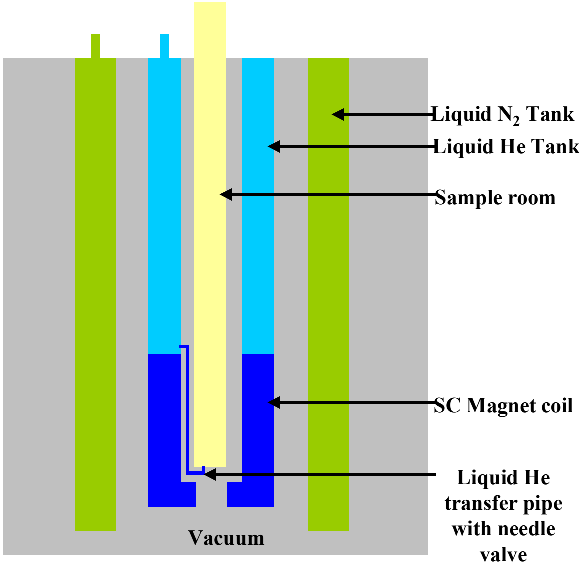

Fig 4.9. Schematic diagram of a liquid He cooled cryostat showing the cryogenic fluid tanks and the superconducting magnet. Also shown in the middle is the sample room.

The TMR samples are glued with rubber-cement onto a 44-pin gold plated chip carrier. The contacts from the chip carrier to the individual electrodes of the TMR junctions are made with Al wires by using an ultrasonic bonding machine. The chip carrier is then fitted into the sample holder. The sample heating in the sample room is done via a resistive coil wound on the sample holder cover.

4.5.2 XPS

To have a better insight and control over the tunneling process it is essential to monitor the oxidation process of the barrier layer with another in-situ characterization technique, which in our case was done by means of X-ray photoemission spectroscopy (XPS). XPS is a very popular, highly surface sensitive technique and is ideally suited for the investigation of the chemical state of the 1-2 nm thick oxide barrier layers employed in tunnel junctions.

In the year 1887 Heinrich Hertz [4.4] observed that metals on being irradiated with UV light emit electrons with kinetic energies which are proportional to the frequency of the incident light frequency. Albert Einstein in 1905 making use of Planck's quantization hypothesis (1900) was the first to give an explanation of the photoelectric effect [4.5]. Assuming elastic scattering and applying the law of conservation of energy one gets the following expression for the kinetic energy (E_{kin}) of the photo-emitted electrons in terms of the binding energy (E_{bin}) of the electrons, quantum of photon energy ($h\nu$) and the work function of the material Φ

$$E_{kin} = h\nu - E_{bin} - \Phi \qquad 4.2$$

Fig 4.10 a) depicts graphically the process of photoemission of a core level electron by a photon. Fig 4.10 b) shows the energy of the incident photon and the energy levels corresponding to Eqn. 4.2.

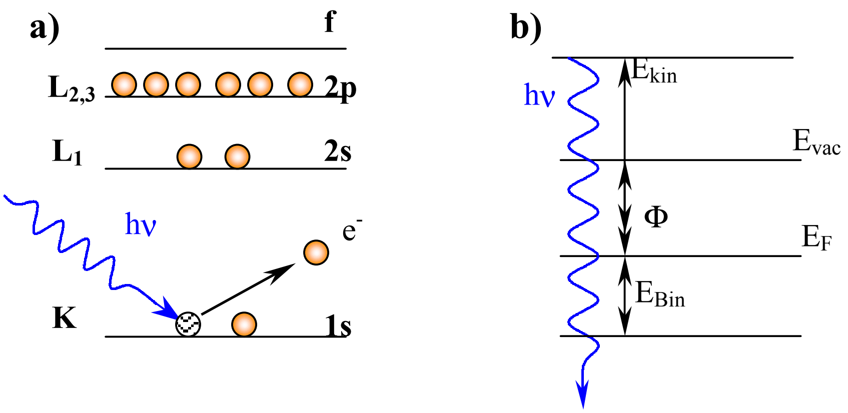

Fig 4.10 The photoelectric effect showing the emission of a 1s core level electron in a) and in b) the energy level diagram

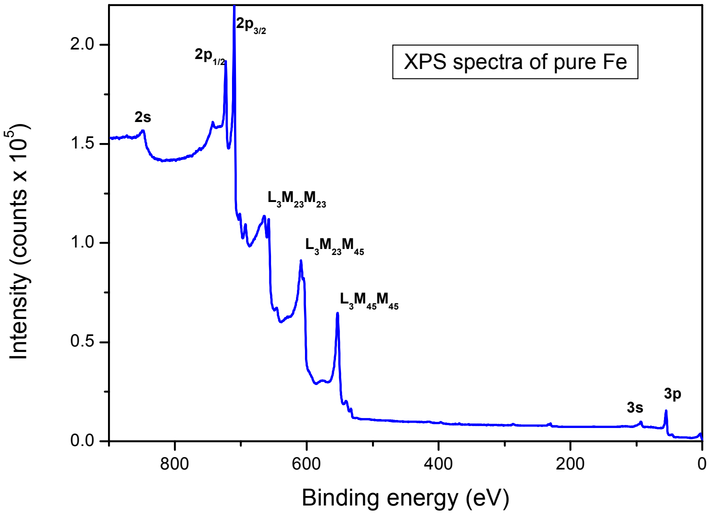

Fig. 4.11. The XPS spectra of a pure 20 nm Fe film showing the characteristic core level peaks and the Auger peaks with reference to E_F.

Shown in Fig 4.11 is an XPS spectrum of a pure Fe film showing the characteristic 2s, 2p doublet, 3s and 3p doublet levels at binding energies of 847, 723, 710, 93, 56 and 55 eV, respectively. Besides the core level peaks one also sees additional peaks at binding energies 659, 608 and 553 eV. These are the LMM core level Auger transition peaks of pure Fe. Fig. 4.12 shows schematically the process of an Auger electron emission. Shown in Fig. 4.12 a) is an atom in an excited state after a K level electron has been photo-excited. After a time of approximately 10^{-14} a higher core level electron L1, Fig. 4.12 b), makes a transition to the unoccupied core level (K) and in this process another electron from a core level is photo-emitted (L_{23}), leaving the atom in a doubly charged state. The Auger transition depicted in b) is designated as a KL_1L_{23} transition. The energy of the Auger electrons is characteristic of the material because it is the difference in the energy of the singly charged initial state and the doubly charged final state.

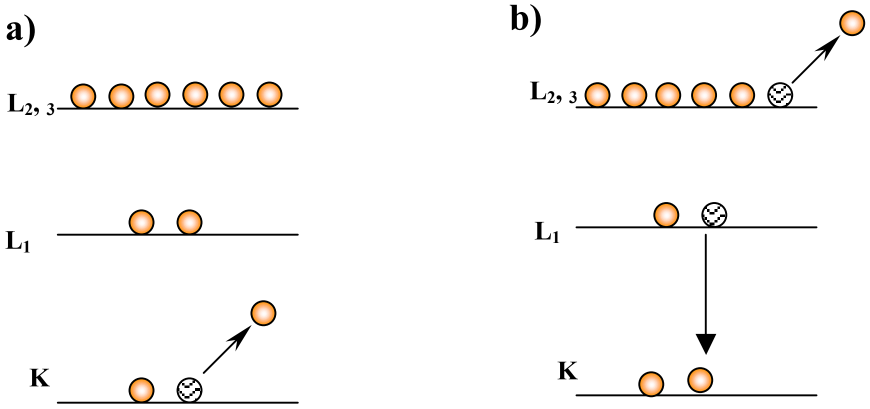

Fig. 4.12. Shown in a) is the singly charged ion after a photo-excitation process. In b) the singly charged ion relaxes to a lower energy state by a L_1 electron filling the hole in the lower K level and in the process imparting the excess energy to a L_{23} electron which is photo-emitted with a characteristic Auger energy. In the final state the ion is doubly charged.

Thus XPS is highly element specific and each element has peaks at characteristic energies corresponding to the different core-levels and the Auger transitions [4.6].

The XPS spectra are obtained by irradiating the sample Fig 4.13 with X-rays, which in our case was the characteristic Mg K_α radiation of energy 1253.6 eV under conditions of UHV. The photo-emitted electrons from the sample surface are then energy analyzed in an electron energy analyzer to obtain the number of counts as a function of the energy or the binding energy of the electrons.

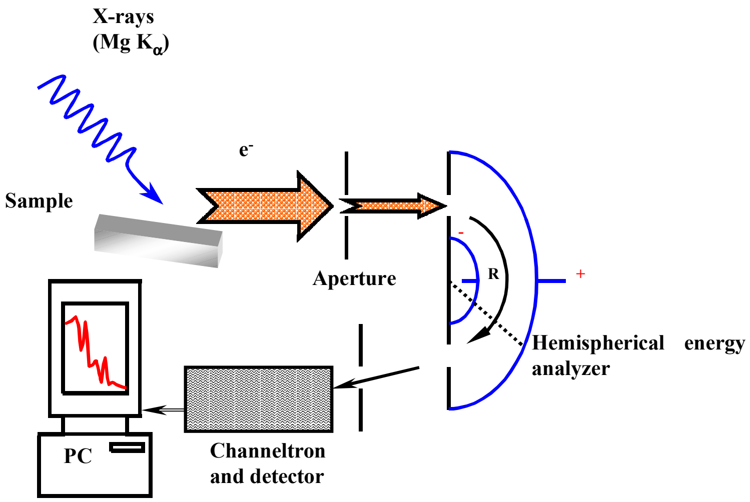

Fig 4.13 Schematic diagram of the XPS analysis set-up showing the X-ray source, sample, and the hemi-spherical electron energy analyzer.

The XPS core levels are also sensitive to the oxidation state of the metal (here Al) film under consideration and one sees changes in the peak shapes and positions of the peaks.

The XPS technique is a highly surface sensitive technique because even though the X-ray penetration depth extends several μm into the bulk. The inelastic mean free path of the photo-emitted electrons in the solids is typically 2 nm only. This is because the probability of the interaction of electrons with matter is much larger than the probability of interaction of photons with matter. The information depth of XPS is therefore only about 2 nm only [4.7].

The XPS spectra of the oxidizing metal layer (here Al) thus enabled the direct correlation of the transport properties of the tunnel junctions with the oxidation state of the barrier.

4.5.2.1 Inelastic background subtraction

It is well known that in order to make good peak shape and quantitative analysis of the X-ray photoemission spectra it is necessary to remove the inelastic contribution to the total intensity of the spectrum [4.8, 4.9].

The inelastic mean free path of electrons in solids is of the order of a few nms, therefore besides the elastic scattering processes the photoemitted electrons also undergo inelastic scattering processes. The inelastically scattered electrons are then photoemitted from the solid with an effectively reduced kinetic energy which manifests into an inelastic tail seen on the higher binding energy side of the core level peaks.

In this work we have extensively used the Tougaard inelastic background subtraction method [4.9]. If j(E) is the experimentally measured spectra and F(E) the spectra obtained after the Tougaard background subtraction

$$\int_{E}^{\infty} \frac{BE'}{(C+E'^2)^2} j(E')dE' \qquad 4.3$$

where B = 2866 eV^2 and C = 1643 eV^2. Thus the background subtracted spectra

$$F(E) = j(E) - \int_{E}^{\infty} \frac{BE'}{(C+E'^2)^2} j(E')dE' \qquad 4.4$$

In this work the Tougaard background subtraction was made using the free software XPSPEAK Version 4.1 by Raymund Kwok. The software is freely available for download.

4.5.2.2 Gauss Lorentz sum peak fits

The background subtracted spectra I_{GL} were then fitted with Gauss+Lorentz sum functions (GL) of the type

$$I_{GL}(E, E_0, w, h, m) = h\left\{(1-m)e^{-\ln Q} + \frac{m}{1+Q}\right\} \qquad 4\ .5$$

where

$$Q = \left[\frac{2.(E-E_0)}{w}\right]^2 \qquad 4.6$$

E denotes the binding energy, E_0 the center of the peak.

The fit paramteres are defined as follows

M is a number between 0 and 1 indicating the % of Gauss function in the sum. m = 0 corresponds to a purely Gaussian fit and m = 1 corresponds to a purely Lorentzian fit. The FWHM of the peak is denoted by *w*.

4.6 Deposition and preparation of epitaxial tunnel junctions

The epitaxial Fe(110)/MgO(111)/Fe(110) tunnel junctions in Fig 4.14 were obtained by first depositing a 20 nm Mo(110) buffer layer on a sapphire Al_2O_3(11-20) substrate.

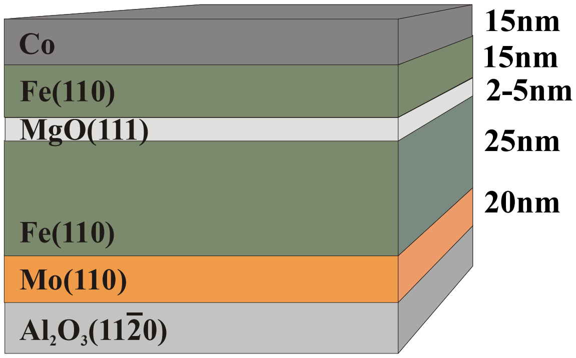

Fig 4.14 The epitaxial Fe (110/MgO(111)/Fe(110) multilyers grown on a sapphire substrate with a Mo(110) buffer layer

The Mo(110) layer is obtained by depositing 20 nm Mo on the sapphire substrate held at a temperature of 700 °C. A 25 nm Fe is then deposited on the Mo(110) at room temperature followed by an annealing stepat 350 °C for a time of 30 min to yield Fe (110). The insulating barrier of MgO is then evaporated with an e- beam evaporator on the Fe (110) layer held at room temperature. The MgO layer has the (111) orientation. The second FM layer is again Fe (110) deposited at room temperature on top of the MgO (111) insulating barrier layer and then followed by annealing at 350 °C. The topmost Fe (110) layer is finally covered by a Co layer so that the switching fields of the two Fe

(110) layers/electrodes are made different. The details of the growth studies are given in [4.10]

5 Results and Measurements

In the initial stages of the study the oxidation of the Al layers was carried out with the help of a low power (15W) in-situ UV lamp and the junctions were defined by depositing the individual layers through shadow masks. The UV light-assisted oxidation in these cases was indirect, i.e. the UV light was not directly incident on the Al layer and the pressure in the oxidation chamber was 1013 mbar (760 Torr or 1 Atm) and the gas flow rate was 0 l/sec. We call this initial study as the pilot study. The results of this are presented in Section 5.1. Later on, in order to reduce the oxidation times and to study the effect of direct UV light irradiation on the oxidation process, the oxidation studies were carried out with a high power 100W USHIO Excimer UV light source (λ = 172 nm, E= 7.179 eV) together with a feedback control loop to precisely control the gas pressure in the chamber. The gas flow rate was also monitored and controlled by regulating the gas inlet pressure and the pumping power. The results of these studies are presented in Section 5.2. In Section 5.3 are presented the results of the tunneling measurements of the epitaxial Fe (110)/ MgO (111)/ Fe (110) tunnel junctions.

5.1 Pilot study

5.1.1 Oxidation of 2nm Al layer

As mentioned previously the barriers for these studies were made with the following parameters while varying the oxidation times.

1. Gas pressure P_{O_2} = 1013 mbar (760 Torr or 1 Atm).
2. Indirect UV light-assisted oxidation.
3. Gas flow rate, F_G = 0 l/ sec.
4. Al metal layer to be oxidized for barrier having thickness 2 nm (nominal as deposited).

The samples employed for the XPS studies were deposited without a shadow mask and each sample, substrate Si(100)/Co(20 nm)/Al(2 nm), was freshly prepared for the different oxidation times t_{Ox}. Shown in Fig. 5.1 are the XPS spectra of the Al 2p core level for the different oxidation times t_{Ox}.

It is clearly seen that as the oxidation time increases the intensity of the Al 2p core level peak at the binding energy 72.2 eV decreases and the intensity of the AlO_X peak at the higher binding energy increases. For the sample with a t_{Ox} = 60 minutes the AlO_X 2p core level peak at the binding energy 74.4 eV indicates that the Al layer could be completely oxidized. The shape and position of the AlO_X core level peak shows no changes for higher oxidation times. Since it is essential that the Al layer is completely oxidized and at the same time the underlying Co layer is not oxidized we monitor the Co $2p_{1/2}$ and Co $2p_{3/2}$ core level peaks at the binding energies 799.5 and 784.4 eV as shown in Fig. 5.2. It can be seen that for t_{Ox} up to 60 min no changes are seen in the shape and position of the peaks. For higher oxidation times, e.g., t_{Ox} = 65 minutes one sees the emergence of a CoO peak at a higher binding energy (+1.6 eV). This is evident from a comparison of the XPS spectra with the CoO reference peak shown in Fig. 5.2. We can therefore from Fig. 5.1 and Fig. 5.2 conclude that under the given conditions the optimum oxidation time of the 2 nm Al layer is around 60 minutes.

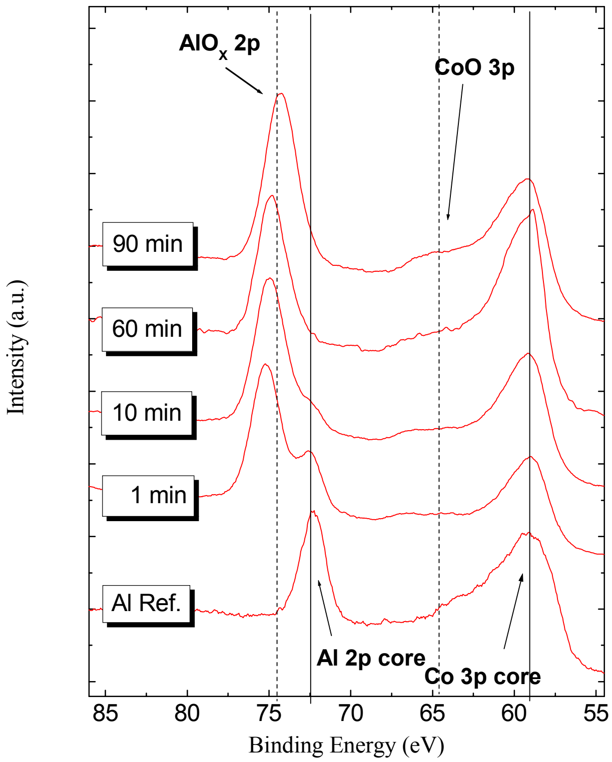

Fig. 5.1. XPS spectra of the Al 2p and Co 3p core levels for different oxidation times. Optimum oxidation time of the nominal Al layer thickness of 2 nm is around 60 minutes. Lower oxidation times show a residual Al core level intensity at the binding energy of 72.2 eV.

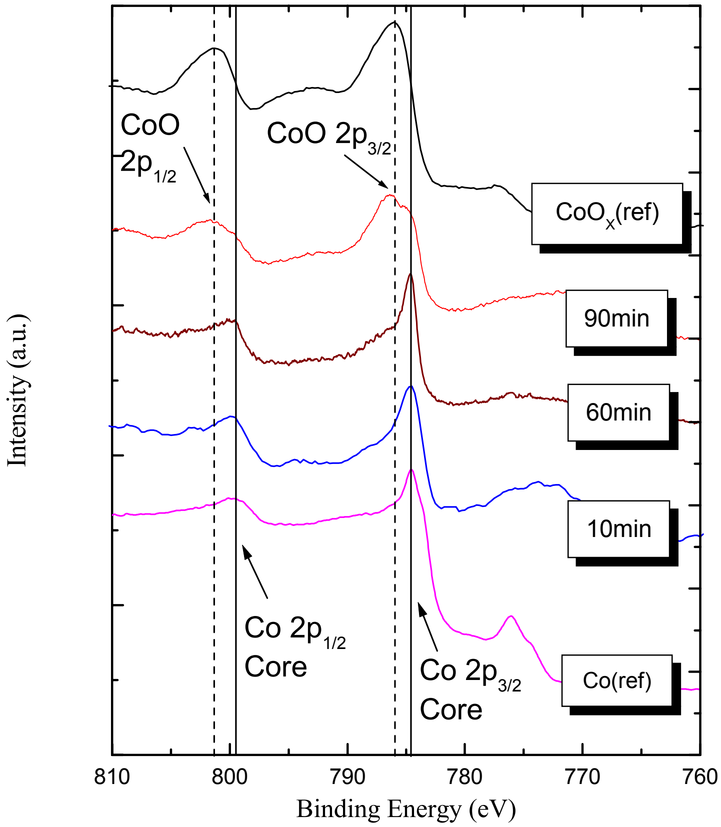

Fig. 5.2. The XPS spectra of the Co $2p_{1/2}$ and the Co $2p_{3/2}$ core levels showing no changes in the peak shape and position for oxidation times t_{Ox} up to 60 minutes. The spectra of higher oxidation times show a similarity to the CoO reference spectra.

On detailed observation of Fig. 5.1 it is seen that the AlOx peaks of the 1 and 10 min oxidized Al layers are shifted slightly to the higher binding energy as compared to the AlOx peaks of the 60 and 90 min oxidized Al layers. The chemical shift of the AlOx 2p core level to the higher BE in the under-oxidized Al layers could be attributed to the charging effects during XPS measurements, however this is ruled out in our case as we do not see a corresponding effect for other core levels or even at the Fermi level. As elaborated in chapter 2 the Cabrera Mott theory of thin film oxidation begins by postulating physisorbed O^- at the gas-initial oxide interface. We here further suggest that the physisorbed O^- could lead to the formation of complex AlOx molecule of the type Al_2O_{3+x} in which the oxidation state of the Al ions is higher than 3+. We now try to analyze the XPS spectra by assuming that the total peak intensity after background subtraction is the sum of the individual peaks due to Al_2O_{3+x}, Al_2O_3 and Al and that the binding energy of the electrons in the Al 2p core level of Al_2O_{3+x} is slightly higher than that of Al_2O_3. Such an assumption would be reasonable given the impossibility of O species' diffusion at low temperatures.

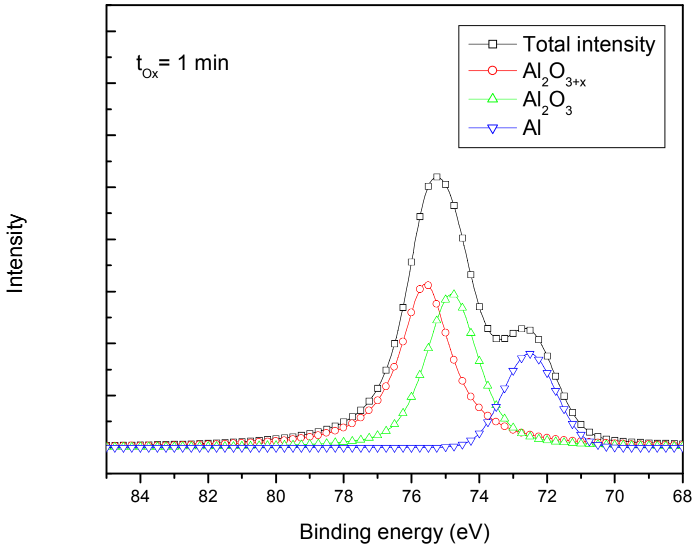

Fig. 5.3. The background-subtracted spectra of a 1 min oxidized 2 nm nominal Al layer and the Gauss Lorentz sum fits showing the individual peaks corresponding to Al_2O_{3+x}, Al_2O_3 and Al

Secondly, switching off the UV lamp and pumping down the oxygen-ozone gas mixture in the chamber reduces the amount of O species available at the interface. This then directly results in the attenuation of the electric potential growth across the oxide layer, which then results in a termination of the transfer of Al ions from the oxide-aluminium interface.

We assume that such a surface layer gets "frozen" on switching off the UV lamp and on pumping out the oxygen-ozone mixture in the oxidation chamber. A prolonged oxidation time helps in maintaining the potential across the barrier and gives the metal ions at the interface sufficient time to tunnel to the surface where they are oxidized to form the oxide. A sufficiently long UV light-assisted oxidation time consequently changes the Al_2O_{3+x} to Al_2O_3. Fig. 5.3 shows the XPS spectra of a 1 min oxidized Al layer in the binding energy range 84-68 eV after a Tougaard background subtraction [5.1] (See Sec. 4.5.2.1.)and Gauss Lorentz sum fits (See Sec. 4.5.2.2). The background subtracted spectrum (total intensity) is fitted with three peaks at binding energies 75.6, 74.8, 72.5 eV corresponding to the Al 2p core levels in the Al_2O_{3+x}, Al_2O_3 and Al species respectively. A plot of the percent of unoxidized Al intensity as a function of UV light-assisted oxidation time t_{Ox} is shown in Fig. 5.4. The percent of unoxidized Al in the XPS spectra is obtained my making a Tougaard background subtraction and by fitting three Gauss Lorentz sum curves as described above. It is evident from the exponential fit that the rate of decrease of the intensity of the Al component after 1 minute of oxidation time falls off exponentially with a characteristic t_{Ox} of 14.58 sec and that the Al component of the intensity is only about 18% after a t_{Ox} of 1 minute.

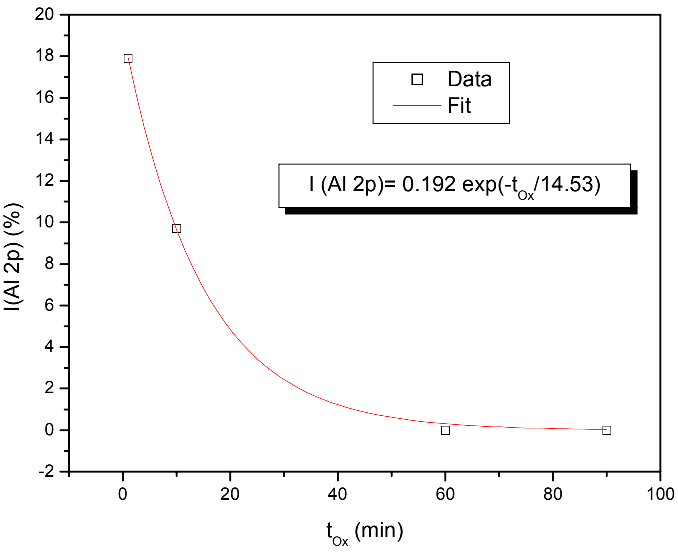

Fig. 5.4 A plot of the intensity of the unoxidized Al 2p core level as function of the UV light-assisted oxidation time. The continuous line is an exponential decay fit to the data.

Attempts to fit two or more peaks into the 60 and 90 min spectra only give peaks whose positions and FWHM correspond neither to Al nor to Al_2O_3. The best fits to the 60 and 90 min spectra are obtained by fitting a single peak of FWHM 2.2 eV at a binding energy of 74.8 eV which agrees very well with the values obtained from a sapphire(Al_2O_3) substrate.

5.1.2 Shadow mask junctions.

Once the optimum oxidation time of the 2 nm Al layer had been determined, the next step was to make tunnel junctions defined by shadow masks. The tunnel junctions were made by first depositing a 20 nm Co layer on a Si(100) substrate through shadow mask 1 followed by a deposition of a 2 nm Al layer through shadow mask 2, oxidizing the Al layers in the load lock chamber for different values of oxidation time. Finally a 10 nm Co layer is deposited through the shadow mask 3 to define the upper FM electrode. The junctions areas were 150 x 150 μm^2.

Shown in Fig. 5.5 are the TMR curves of an optimum oxidized junction at a temperature of 10, 100 and 285K showing a large *TMR* of 31, 36 and 13%, respectively. It can be seen that the magnitude and the shape of the *TMR*s and the curves respectively change with changing temperature. The TMR is a maximum at 100 K and a minimum at 285 K. Besides it can also be seen that the maximum field required for parallel alignment of the two FM layers increases with decreasing temperature from 0.01 tesla at 285 K to 0.4 tesla at 10 K. We attribute these observations to an approximately 2nm thick CoO layer formation of the top Co layer when exposed to air. This CoO layer exchange biases the top Co layer to modify its coercive field with temperature [5.2]. The coercive fields of the two FM layers are at 285 K very close to each other and could therefore reduce the *TMR*. At a temperature of 100 K the coercive fields are well separated making it possible to realize nearly complete anti-parallel alignment of the two FM layers. However, at 10 K, in spite of the increase in coercive field of the top Co layer, we see that the *TMR* is smaller than that at 100 K. This can be explained by noting the greater spread of the TMR curves on the high field sides due to the exchanged biased top Co layer.

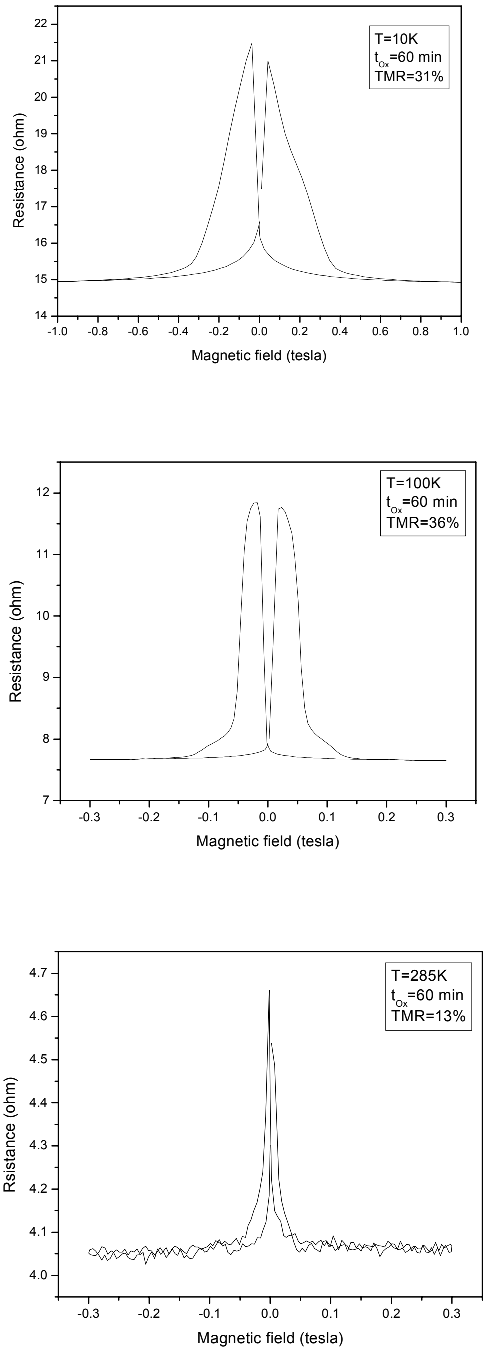

Fig. 5.5. TMR curves of a 60 min oxidized barrier at temperatures of 10,100 and 285 K exhibiting *TMR*s of 31, 36 and 13%, respectively.

The greater spread of the hysteresis curve of the exchange biased upper Co layer results in the overlap of the hysteresis curves of both the Co layers resulting in a poorer anti-parallel alignment. The *TMR* is therefore lower at 10 K. Plotted in Fig. 5.6 are the *TMR*s of the junctions as a function of the UV light-assisted oxidation times at a temperature of 100 K. It can be seen that the *TMR*s of the optimum oxidized junction $t_{Ox} = 60$ min shows a maximum *TMR* of 36% and the under-oxidized and over-oxidized samples, e.g. for 45 and 75 min show much smaller *TMR*s of about 20%. In the case of the under-oxidized samples this reduction is due to the presence of unoxidized Al at the Co/AlOx interface which destroys the spin polarization of the tunneling electrons or due to the presence of unoxidized Al within the barrier. The presence of such unoxidized Al in the barrier could lead to inelastic tunneling via defect states in the barrier which again reduce the effective spin polarization of the tunneling electrons.

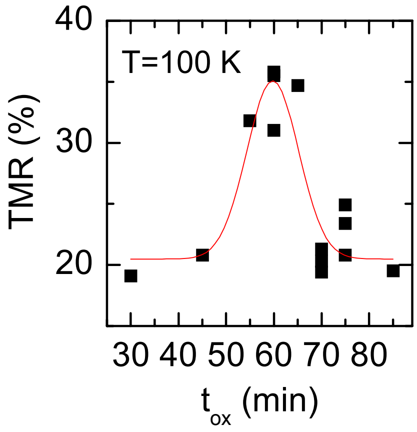

Fig. 5.6. A plot of the *TMR*s at a temperature of 100 K as a function of the indirect UV light-assisted oxidation times of the 2nm Al barrier layer.

In case of the over-oxidized samples, the XPS spectra clearly show the presence of oxidized Co at the Co/oxide barrier interface. The presence of such oxidized Co also reduces the effective spin polarization of the tunneling electrons [5.3, 5.4]. Besides, it is known that CoO is anti-ferromagnetic at low temperatures.

A similar plot at a temperature of 285 K in Fig. 5.7, however, shows that the reduction of the *TMR* is much more pronounced in the case of the under-oxidized than for the over-oxidized junctions. It can therefore be noted from Fig. 5.6 and Fig. 5.7 that over-oxidation of the barriers is less detrimental to the *TMR* of the junctions as compared to under-oxidation of the barriers.

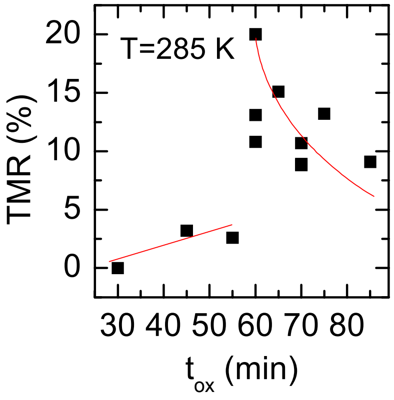

Fig. 5.7. A plot of the *TMR*s at a temperature of 285 K as a function of the indirect UV light-assisted oxidation times of the 2nm Al barrier layer.

Shown in Fig. 5.8 are the *R* vs. *T* curves of two junctions as a function of the temperature. It can be seen that the Rowell criteria of insulator-like *R* vs. *T* is satisfied by a junction with a 65 min oxidized barrier which exhibits tunneling whereas even an over-oxidized barrier (75 min.) junction most likely due to pinholes shows a metallic R vs. T characteristic. The temperature dependence of the resistance or conductance of the junctions is discussed in further detail later in section 5.1.5.

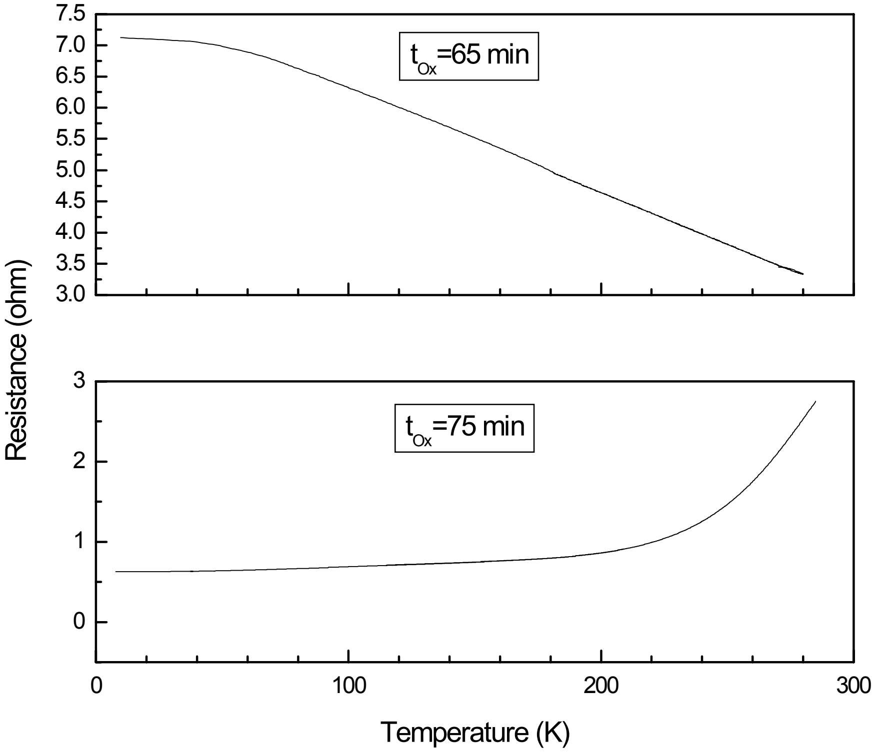

Fig. 5.8. Plotted on top is the *R* vs. *T* curve of a junction which exhibits insulator-like behaviour thus satisfying Rowells criteria and below of an over-oxidized barrier with presumably pinholes in the barrier manifested by a metallic *R* vs. *T* behavior.

5.1.3 Microstructured junctions

In this section the results of measurements of junctions defined by microstructuring are presented. The oxidation parameters remain the same as in the previous section namely

1. Gas pressure P_{O_2} = 1013 mbar (760 Torr or 1 Atm).
2. Indirect UV light-assisted oxidation.
3. Gas flow rate, F_G = 0 l/ sec.
4. Nominal Al metal layer thickness 2 nm to be oxidized for making the barrier.

The junction areas were 400 μm² and a total of 30 junctions were defined by microstructuring. The junctions with an indirect UV light-assisted barrier oxidation time t_{Ox} of 65 min, i.e. optimum oxidized barrier, shows a maximum *TMR* of 9.5% at 280 K (Fig. 5.9 a) and the corresponding R×A product is 1920 kΩμm². The maximum observed *TMR* at 100 K is 14% (Fig. 5.9 b) and again as observed in the case of the shadow mask deposited junctions the maximum observed *TMR* at 4.2 K of 13% is smaller than the *TMR* observed at 100 K. Shown in Fig. 5.10 is the *R* vs. *T* curve of a typical microstructured junction, which clearly satisfies the Rowell criteria of insulator- like *R* vs. *T*. The temperature dependence of the resistance or conductance is discussed in further details in section 5.1.5.

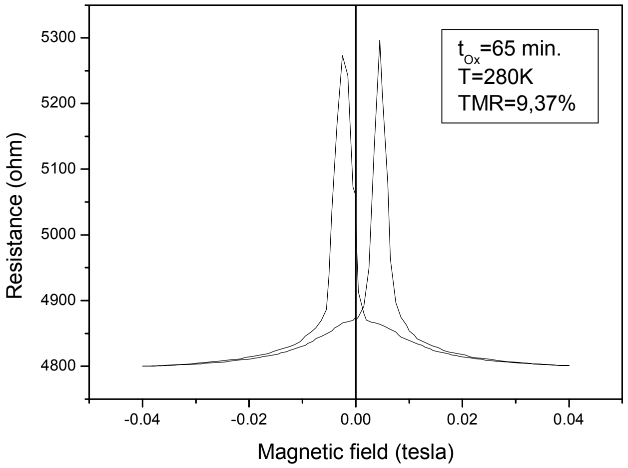

a)

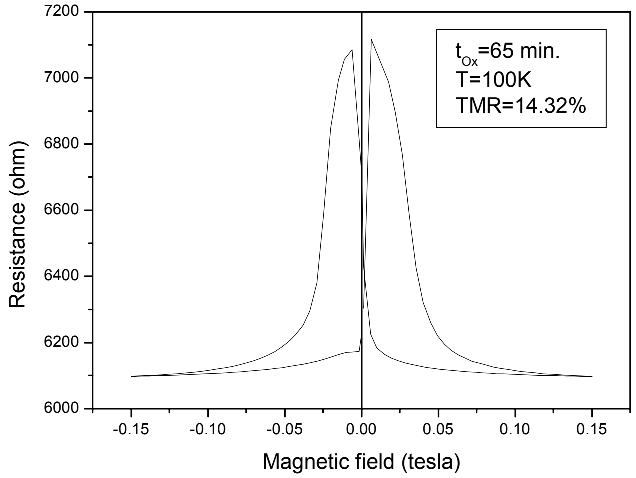

b)

Fig. 5.9. Shown above in a) the maximum observed *TMR* of 9% at 280K and below in b) the maximum *TMR* of 14% at 100 K of the microstructured junctions Co(10 nm)/Al(2 nm + t_{Ox} 65 min)/Co(20 nm)/Si(100) substrate (Sample AR06).

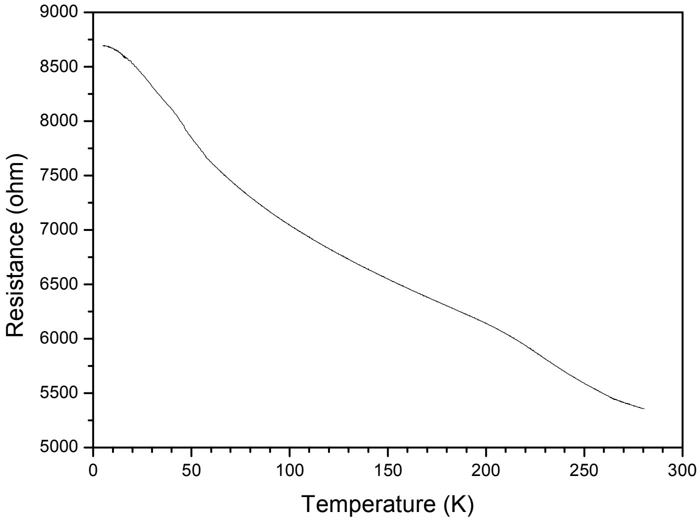

Fig. 5.10 The *R* vs. *T* curve of an optimum oxidized micro-structured junction (Sample AR06) satisfying Rowells criteria of insulator-like *R* vs. *T*.

Shown in Fig. 5.11. are the *TMR*s at a temperature of 280 K plotted versus the resistance of the micro-structured junctions (Sample AR06) with a barrier oxidation time t_{Ox} = 65 min. At 280 K the maximum observed *TMR* is about 9.5%. It is observed that most of the junctions having a resistance in the range 3 – 7 kΩ exhibit larger *TMR*s and the *TMR*s vary from 4 to10%. None of the junctions show a resistance in the range 300-2500 Ω. The junctions having a resistance lesser than 300 Ω show MR effect of less than 0.5%. Such junctions most likely have metallic shorts or pin-holes between the two Co layers. These will be dealt with in further details in the next section.

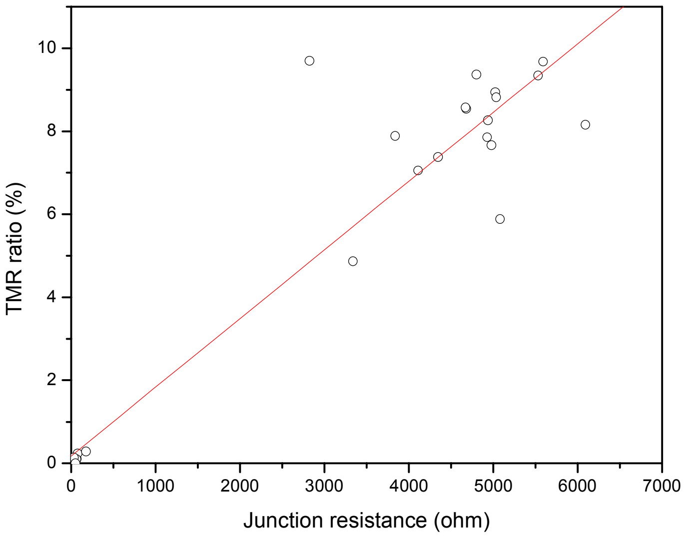

Fig. 5.11. A plot of the *TMR* versus junction resistance at 280 K showing a maximum *TMR* of 9.5%.

Plotted in Fig. 5.12. are the number of “good” junctions i.e. junctions which exhibit resistances greater than 2 kΩ and satisfy the Rowell criteria versus junction resistance. The resistance of the junctions vary from 3 to 6 kΩ and the *TMR* varies from 5% to 9.5%. The mean junction resistance R is 4700 Ω, Thus giving a mean R×A product of 1880 kΩμm^2. Shown in Fig. 5.13 is the statistics of all the 30 junctions of the sample AR06 as a function of the junction resistance. It is seen that 50% of the 30 microstructured junctions have resistances lower than 1000 Ω and such junctions exhibit very small or no *TMR*.

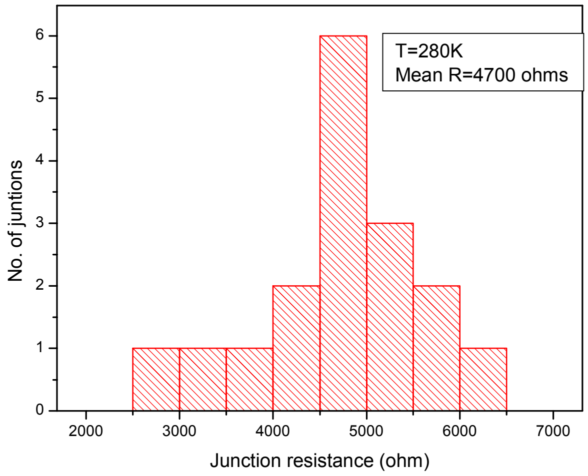

Fig. 5.12 Plot of No. of “good” junctions (Sample AR) versus junction resistance. The junctions have a mean resistance of 4700 Ω.

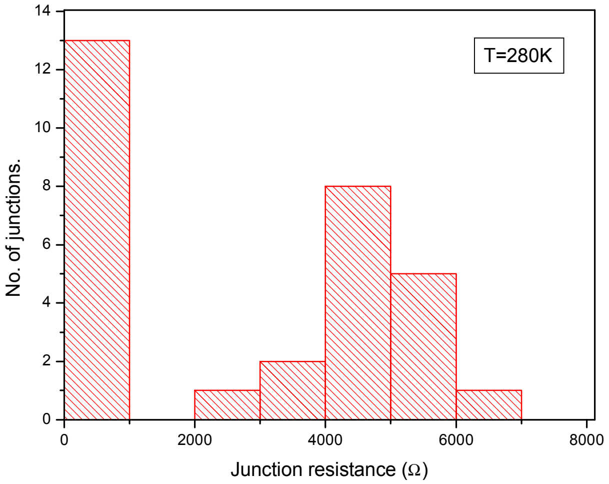

Fig. 5.13 Statistics of all the 30 junctions (Sample AR) showing the No. of junctions as a function of the resistance. The 13 “bad” junctions can be seen in the leftmost column and have resistances less than 1 kΩ.

A plot of the number of junctions versus the observed *TMR* in Fig. 5.14. shows that most of the junctions have a *TMR* ranging from 7 to 10% with a mean *TMR* of 8.1%.

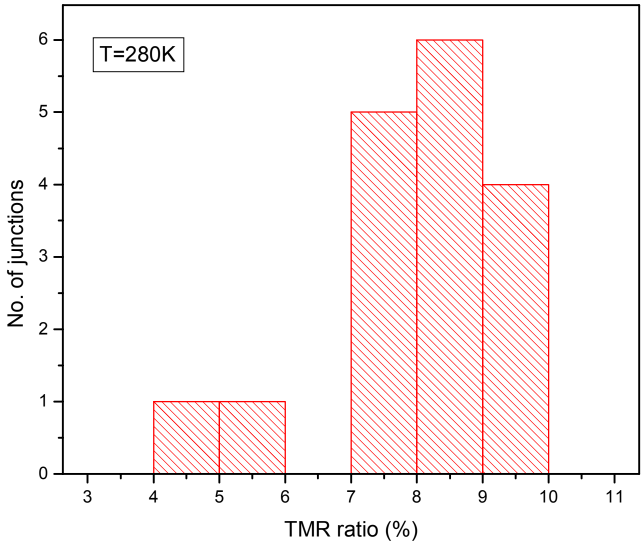

Fig. 5.14 Statistics of the *TMR* of the junctions which exhibit tunneling. The mean *TMR* is 8.1%.

5.1.4 Barriers with shorts or pin-holes

It is generally believed that a single short or pin-hole across the junction barrier is sufficient to completely obliterate the *TMR* effect. We present here evidence that even though a pin-hole or a short considerably reduces the *TMR* it is still possible to observe a small Magneto-resistance (MR) effect. We present here evidence that even for the junctions with pin-holes or shorts it is still possible to observe a TMR of about 0.4%. Fig. 5.15 a) and b) shows the MR curves of two such low resistance junctions with shorts. Such junctions exhibit a small MR ratios typically 0.1 to 0.4%. Shown in c) is the TMR curve of a junction which shows tunneling behavior. The similarity, especially the presence of the resistance peaks in a) and b) at magnetic fields similar to those in c)

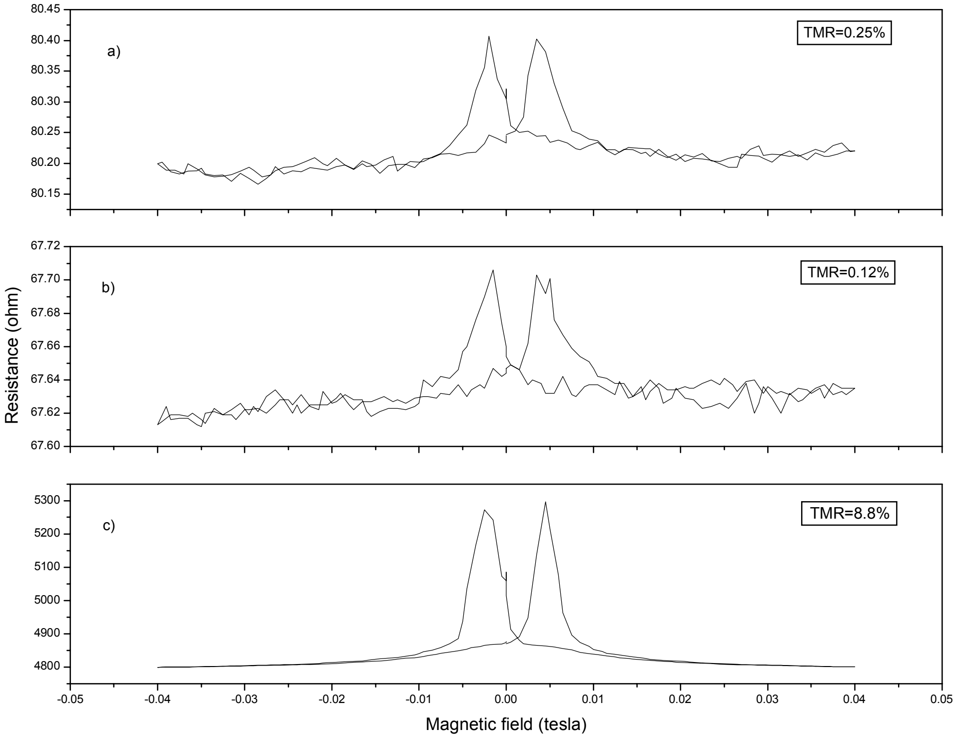

Fig. 5.15 TMR curves of two junction with shorts a) and b) and one without a short c) all showing similar hysteresis curves except for the magnitudes of the *TMR*s.

makes it clear that even though the junctions in a) and b) have shorts in their barriers they still show a finite MR effect.

The observance of a finite *TMR* can be qualitatively and quantitatively understood by a simple two parallel resistor model. In the parallel resistance model the resistance across the barrier is replaced by two effective resistances connected in parallel Fig.. 5.16.

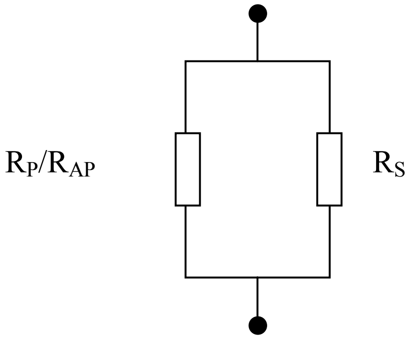

Fig. 5.16 A simple parallel resistor model to explain finite TMR observed in a shorted junction.

One of the resistances simulates the metallic short which exhibits no *TMR* and has a metallic R vs T character. The other resistor simulates the spin dependent tunnel current which exhibits an insulator-like R vs T behavior. We assume a resistance R_S across the short and a resistance $R_P(R_{AP})$ across the barrier without a short in the parallel (anti-parallel) state. On calculating the total resistance across the two parallel resistances one then obtains for the *TMR* in the presence of shorts TMR_S, the following relation in terms of the *TMR* in the absence of any shorts.

$$TMR_S = \frac{\overline{R}_P}{R_P} \times TMR \qquad 5.1$$

where R_P and $\overline{R}_P$ are, respectively, the resistances of the un-shorted and shorted junctions in the parallel magnetized state. On inserting the value of mean R_P as 4700 Ω and the mean *TMR* as 8.1% and the observed $\overline{R}_P$ of 80 Ω we get a TMR_S value of 0.14% which agrees fairly well with the order of magnitude of the observed value of 0.25%. It can therefore be said that if one has junctions with a lower mean value of R_P and high mean *TMR* and if one of the junctions has a short such a junction could still exhibit a measurable and useful TMR_S ratio.

5.1.5 Shadow mask deposited versus microstructured junctions

The results presented in the previous two sections make it clear that the *TMR*s and the R×A products of the shadow mask defined junctions and the microstructured junctions vary significantly. The maximum observed *TMR*s at 280 K were 20% for the shadow mask deposited junctions and 9% in case of the micro-structured junctions.

The average R×A products of the shadow mask deposited junctions were around 90 kΩμm^2 and the mean values of the microstructured junctions were 1880 kΩμm^2. In the next two subsections we examine the probable causes of this discrepancy and also the temperature dependence of the tunnel resistivity and *TMR*.

5.1.5.1 Temperature dependence of the tunnel resistivity

The most interesting difference between the shadow mask deposited and the microstructured junctions can be seen in the temperature dependence of the tunnel resistance. Shown in Fig. 5.17 a) and b) are the typical resistance versus temperature plots of the shadow mask defined and the microstructured junctions. Both the samples are similar in all respects (Co(10 nm)/Al(2 nm + t_{Ox} 65 min)/Co(20 nm)/Si(100) substrate) except for the method of defining the junction area. The R vs. T curves were measured without a bias field (WF) and therefore the possibility of the relative magnetization to the two FM films changing with temperature cannot be ruled out. To verify this and as a guide to the eyes also plotted are the junction resistances at three different temperatures for both the parallel (R_P) and the anti-parallel (R_{AP}) magnetized states.

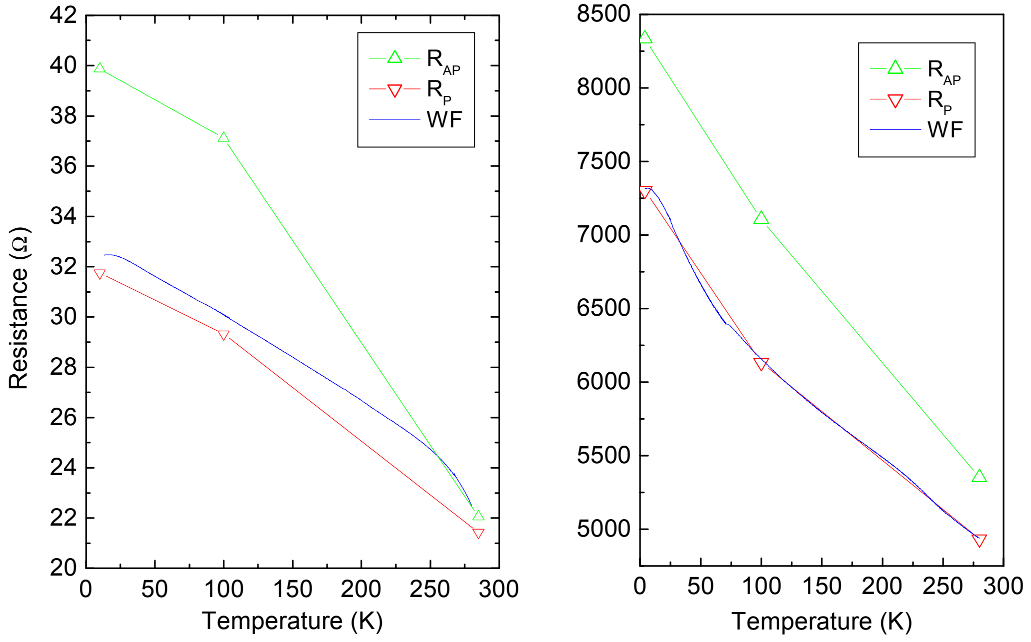

a) Shadow masked **b) Microstructured**

Fig. 5.17 The R vs. T behaviour (lines) of the two types of junctions. Also plotted are the resistances of the junctions in the parallel (down triangle) and the anti-parallel (up triangle)

The prominent causes for the observed differences in the characteristics of the two types of junctions could be twofold. The first cause is the so called Petersen effect which occurs in the four point probe geometry when the resistances of the electrodes are comparable or larger than the junction resistances. The measured resistance is then smaller than the actual resistance of the junction, thus leading to large errors in the resistance and *TMR* values [5.5]. In such cases it is even possible that a negative junction resistance is measured. In the case of our shadow mask deposited junctions this was found indeed to be the case as the electrode resistances were of the order of 100 – 1000 Ω. In the case of the microstructured junctions this problem was eliminated as the electrode resistances were only of the order of 10 Ω which are much smaller than the junction resistances of the order of several kΩ.

The other source and cause of the discrepancy between the results of the shadow mask deposited and the microstructured junctions could be the obvious edge effects in the shadow mask deposited junctions. Shown in Fig. 5.18 is a cross-section sketch of the shadow mask defined junction area.

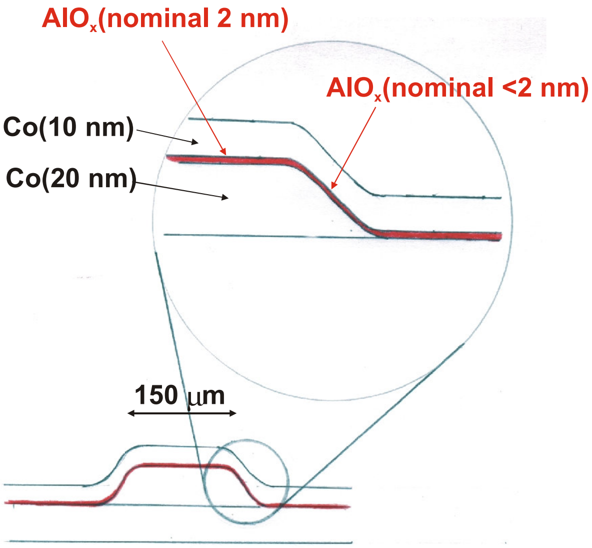

Fig. 5.18. The cross section of a shadow mask defined junction showing the effectively thinner oxide barrier at the edges of the lower Co electrode.

The cross-section is made perpendicular to the length of the lower Co(20 nm) electrode. It is clear here that the thickness of the barrier at the edges is dependent on the width of the edge of the lower Co electrode. A width edge of zero would in principle lead to no deposition of Al along the side-walls of the lower Co electrode. A consequent oxidation would only lead to a formation of a CoO barrier layer at the edges. Such a CoO layer could considerably affect the tunneling process rendering it complex for qualitative and quantitative analysis.

5.1.5.2 Temperature dependence of conductance and *TMR*

Shown in Fig. 5.19 is the temperature dependence of the conductance of the shadow mask deposited junction (Co(10 nm)/Al(2 nm + t_{Ox} 65 min)/Co(20 nm)/Si(100) substrate) shown in Fig. 5.17 a. The data points are the open squares and the line is a Glazman-

Matveev fit to the data. The best fit to the total conductance is obtained by including the conductance terms corresponding to conductance via chains of localized defect states in the barrier with n=1, 2 and 3. It is indeed seen that the temperature dependence of the tunnel conductance can be explained over a wide temperature range in terms of inelastic tunneling via localized defect states as suggested by Glazmann and Matveev (See Section 3.4.1). The ability to estimate the elastic and the inelastic components of the tunnel conductance further enables the evaluation of the *TMR* as a function of temperature. Tabulated in Table 5.1 are the observed *TMR*s of the shadow mask deposited junction and the ratio of the inelastic and the elastic components of the tunnel conductance calculated at different temperatures. As explained in Chapter 3 the calculated *TMR* is obtained by the equation

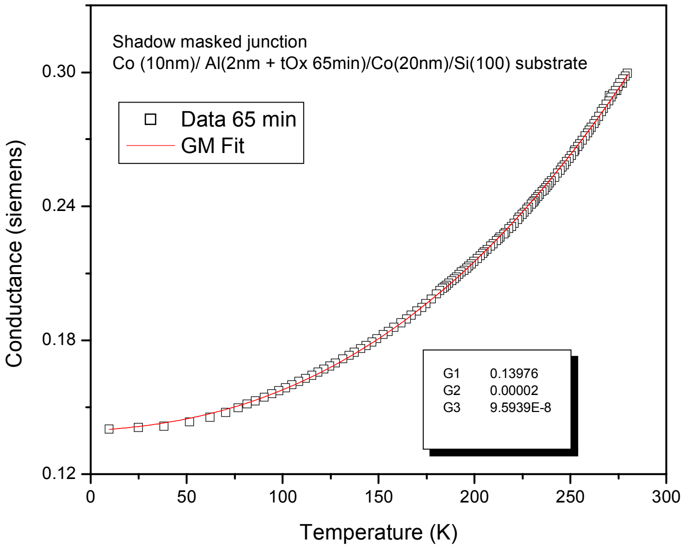

Fig. 5.19 The temperature dependence of the conductance of a shadow mask deposited junction (Co (10nm)/ Al(2nm + t_{Ox} 65min)/Co(20nm)/Si(100) substrate) and the Glazmann-Matveev fit to the data with n=1,2 and 3.

$$TMR_{Calculated}(V,T) = \left(\frac{G_{El}}{G_{El} + G_{In}} \right) TMR_{Observed}(0,0) \qquad 5.2$$

where $TMR_{Calculated}(V,T)$ is the TMR value calculated at a temperature T and bias voltage V and $TMR_{Observed}(0,0)$ is the maxi mum observed TMR at $V,T = 0$ and corresponds to $TMR_{Julliere}$. In calculating the *TMR* at 285 K it is assumed that the *TMR* observed at 100 K is the maximum TMR of the junction. Such an assumption is reasonable considering that form the fit at 100 K, we get $G_{In} = 0.128G_{El}$ (See Table 5.1). The calculated values of 16% agrees well with the *TMR* of 15% observed at 285K.

It is similarly possible to fit the temperature dependence of the tunnel conductance of the microstructured junction with n=1 and 2 i.e. the conductance of the microstructured junctions changes with temperature as $T^{4/3}$ (Eqn. 39, 3.10). On including the term n = 3 the fit quality deteriorates. This is unlike the case of the shadow mask deposited junction where even the terms with n=3 are needed to fit the data.

Shadow Mask Junction	G_{In}/G_{El}	$TMR_{Observed}$ (%)	$TMR_{Calculated}$ (%)
10 K	$3x10^{-3}$	31	31
100 K	0.128	36	-
285 K	1.2	15	16

Table 5.1. The calculated and the observed value of the *TMR* at 285 K of the shadow mask deposited junction shown in Fig. 5.17 and 5.19. The calculated value is obtained by assuming that the maximum *TMR* is observed at 100K.

Tabulated again in Table 5.2 are the observed values of the *TMR*s at 100 K and 285 K.

Microstructured Junction (AR06)	G_{In}/G_{El}	$TMR_{Observed}$ (%)	$TMR_{Calculated}$ (%)
100 K	0.163	14	-
285 K	1.2	9	8.5

Table 5.2 The calculated and the observed value of the TMR at 285 K of a microstructured junction (Sample AR06). The calculated value is obtained by assuming that the maximum TMR is observed at 100K.

Once again since at 100 K, $G_{In} < G_{El}$ we assume that the observed *TMR* of 14 % is the maximum *TMR* that would have been observed in the absence of any inelastic tunneling conductance. At 285 K the ratio G_{In} / G_{El} is 1.2 and the observed *TMR* value is 9% which agrees well with the value of 8.5% obtained from the GM fit and the calculation.

5.1.6 Oxidation of 1.5 nm Al layer

In this section the results of the oxidation of 1.5 nm Al layer are presented. The conditions of oxidation were similar to those of the previous section i.e.

1. Gas pressure P_{O_2} = 1013 mbar (760 Torr or 1 Atm).
2. Indirect UV light-assisted oxidation.
3. Gas flow rate, F_G = 0 l/ sec.
4. 1.5 nm (nominal as deposited) Al metal layer to be oxidized to form the barrier.

The oxidation of the 1.5 nm Al layer proceeds similarly as in the case of the 2 nm Al layer. The XPS spectra of the low oxidation time samples clearly show the shifts to the higher binding energies of the AlOx core level peaks, i.e. there is evidence again of formation of Al_2O_{3+x}. The intensity of the Al 2p core level component falls exponentially with time as seen from the exponential fit in Fig. 5.20. The percentage of the Al 2p core level intensity is obtained after a Tougaard background subtraction and Gauss-Lorentz sum function fits to the XPS spectra of the samples with different oxidation times t_{Ox}. The exponential fit in Fig. 5.20 gives a characteristic oxidation time t_{Ox} of 1.3 min. However unlike in the case of the 2 nm Al layer the oxidation is never complete i.e. a 5% unoxidized Al component is observed even for very high oxidation times. The oxidation of the underlying Co layer is observed for $t_{Ox} > 5$ mins.

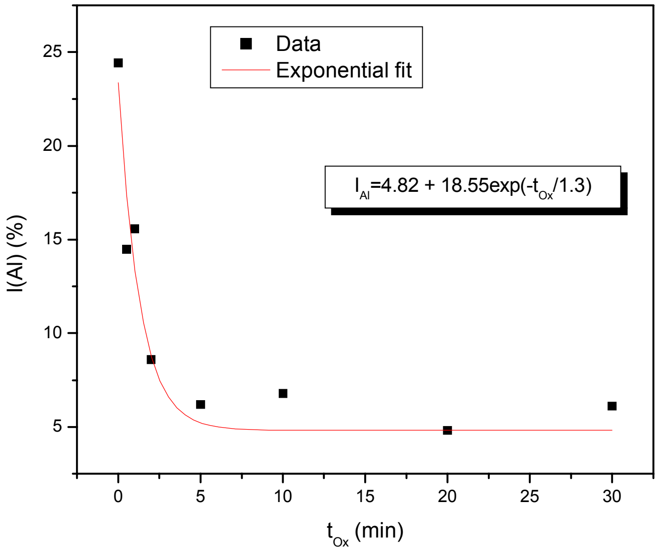

Fig. 5.20 The intensity of the unoxidized Al component as a function of t_{Ox} of a 1.5 nm Al layer. The intensity falls exponentially and saturates at 5%.

5.1.7 Oxidation of 1 nm Al layer

The oxidation studies of a 1 nm Al layer deposited on a Si(100)/Co(20 nm) template proceeds similarly to the oxidation of the 2 and 1.5 nm Al layers described in the previous sections. The optimum oxidation time of the 1 nm Al layer is found to be 30 sec. Higher oxidation times clearly show the emergence of a CoO peak as can be seen from the Co Auger peaks.

5.1.8 Summary

TMR was successfully observed at room temperatures with a 2 nm Al barrier layer. The mean junction resistances and *TMR*s of the shadow mask deposited and microstructured junctions differ considerably. Possible causes for the differences are the Petersen effect and more prominently the edge effects. Clear differences in the temperature dependence of the two types of junctions are observed. In the light of these observations and the advances in junction fabrication techniques it could be useful to repeat and review many of the tunneling experiments carried out in the past.

The maximum observed *TMR* at room temperature in case of the optimum oxidized, 2nm thick Al barrier and microstructured junctions, was about 9.5% and the mean *TMR* of 15 junctions was 8.1%. The *TMR* varied from 5 to 9.5%. Out of a total of 30 junctions each of area 400 μm^2 spread over a distance of 10 mm on the Si(100) substrate, 15 junctions were successfully obtained.

The mean R×A product was 1880 kΩμm^2. Junction resistances vary from 3 to 6 kΩ. 50% of the 30 junctions were shorted and had very low resistances ~ 100Ω. In spite of the shorts such junctions showed a small finite MR ratio ranging from 0.1 to 0.4%.

The temperature dependence of the tunnel conductance could be qualitatively and quantitatively understood in terms of the GM model of tunneling via chains of localized defect states in the barrier. Separating the elastic and the inelastic components of the tunnel conductance leads to a possible explanation of the temperature dependence of the *TMR*.

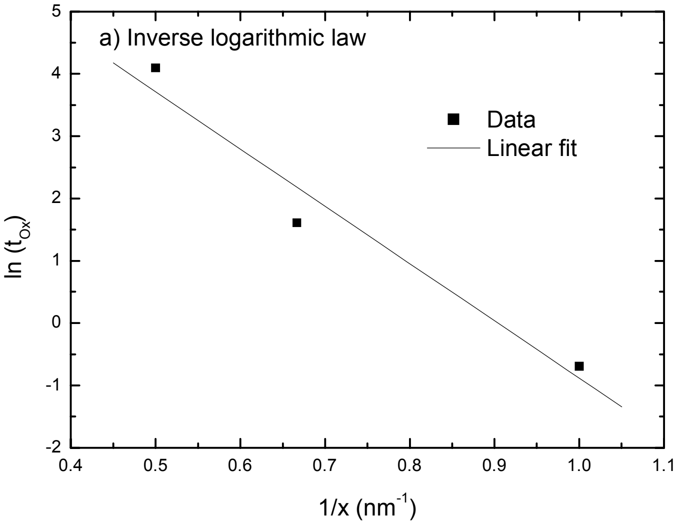

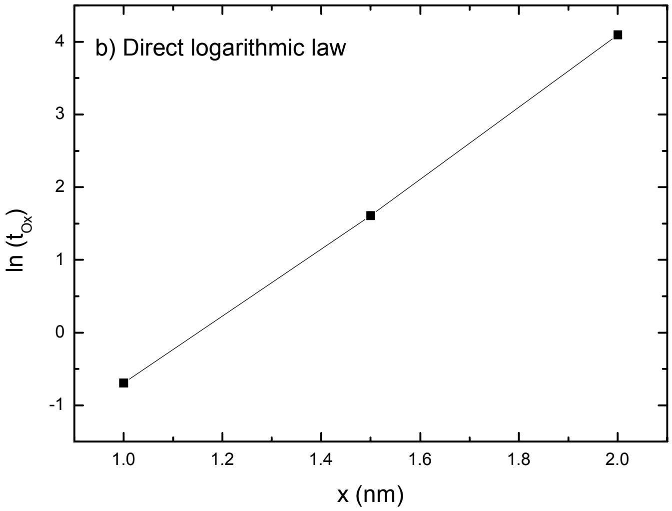

Fig. 5.21 Shown in a) is a logarithmic plot of the optimum oxidation time versus the inverse Al layer thickness corresponding to the inverse logarithmic law. Plotted in b) is ln (t_{Ox}) vs x corresponding to the direct logarithmic law.

The XPS studies of Al layers for different oxidation times and thickness clearly show that the oxidation proceeds via a formation of a complex Al_2O_{3+x} surface layer. Sufficiently long oxidation times then change the Al_2O_{3+x} to Al_2O_3 as more and more cations from the initial oxide-metal interface tunnel to the surface.

The Al 2p core level intensity falls experimentally with t_{Ox}. A logarithmic plot of the optimum film oxidation time vs. the inverse film thickness is shown in Fig. 5.21 a). The agreement with the inverse logarithmic law of Cabrera and Mott (Eqn. 2.19) is good if one allows for a 6% scatter in the film thickness x. However, the agreement with the direct logarithmic law (See Fig. 5.21 b)) is also good. Such a direct logarithmic law has been reported in the past [5.6] and agrees with earlier versions of Mott's theory of thin film oxidation [5.7, 5.8].

5.2 Oxidation with Excimer UV lamp

In this section the results of the oxidation studies carried out with the new high power 100 W USHIO Excimer UV lamp (λ=172nm or E=7.197 eV) are shown. Presented first are the determination of the optimum oxidation time and the oxidation rate followed by a comparison of the direct and indirect UV light assisted oxidation.

The conditions of oxidation were

1. Gas pressure P_{O_2} = 130 mbar (100 Torr.).
2. Direct UV light-assisted oxidation.
3. Gas flow rate, F_G = 4 l/ min.
4. 1 nm (nominal) as deposited Al metal layer to be oxidized for making the barrier.

The 1 nm Al barrier layer used for this study was deposited on epitaxial Fe(110)/Mo (110)/Al_2O_3 (11-20). Depicted in Fig. 5.22 are the Al 2p core level spectra of the 1nm Al films oxidized for different oxidation times t_{Ox} together with the Al 2p Ref. core level peak and the Al core level in Al_2O_3 (sapphire) Ref. spectra.

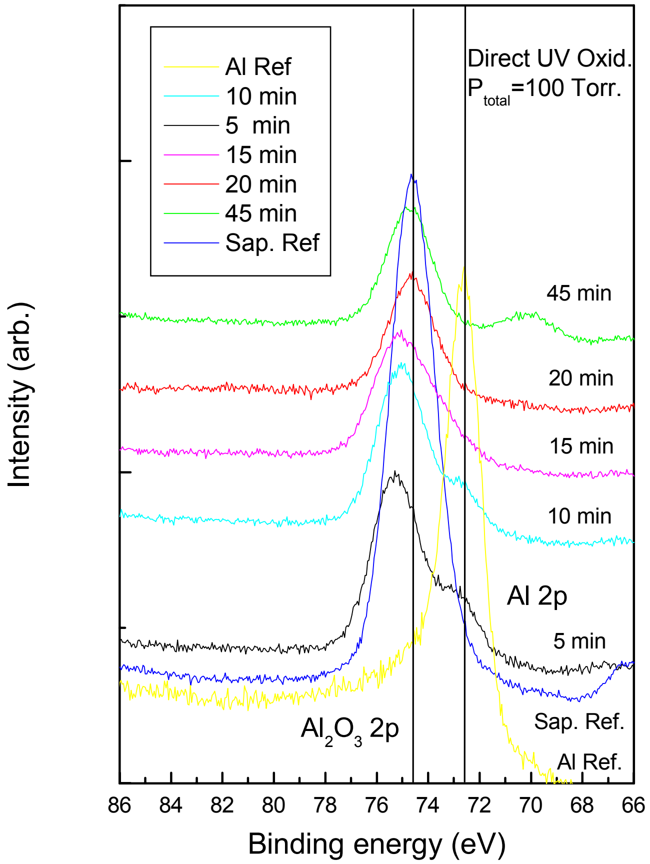

Fig. 5.22. The Al 2p core level spectra for different oxidation times of a 1nm Al layer together with the Al 2p (Ref) and the Al 2p (in sapphire) core levels. With increasing oxidation time the intensity of the Al 2p core levels decreases and that of the chemically shifted oxide peak increases. For t_{Ox} = 20 min the spectrum coincides with the sapphire Ref .

It is seen that the Al 2p level coincides with the Al 2p core level in Al_2O_3 only for a t_{Ox} greater than or equal to 20 min. A t_{Ox} less than 20 min, i.e. 15 min. clearly shows the presence of unoxidized or partly oxidized Al as a shoulder on the low energy side of the peak. Besides it is observed that for t_{Ox} less than 20 min the oxide peak is shifted by a BE of 0.65 eV to the higher BE as compared to the BE of Al in Al_2O_3 .

Again as in the previous section the oxidation proceeds via the formation of a Al_2O_{3+x} surface layer which then consequently changes to Al_2O_3 with higher oxidation times. Shown in Fig. 5.23 is the XPS spectrum of a 10 min UV light oxidized Al layer after a Tougaard background subtraction and with the individual Gauss Lorentz sum peak fits corresponding to the Al 2p levels in Al_2O_{3+x}, Al_2O_3 and Al.

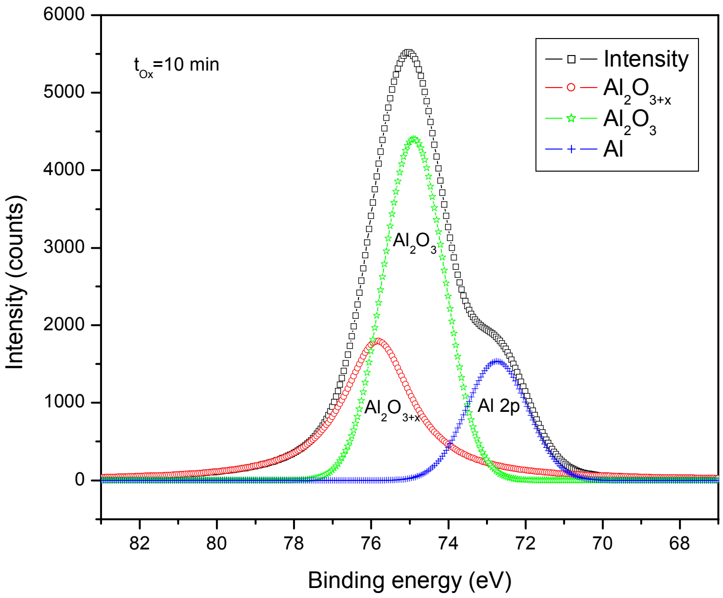

Fig. 5.23 The XPS spectrum of the 10 min oxidized sample of 1nm Al after a Tougaard background subtraction and Gauss Lorentz sum fits corresponding to Al_2O_{3+x}, Al_2O_3 and Al.

The individual Al_2O_{3+x}, Al_2O_3 and Al peaks have binding energies of 75.8, 74.8 and 72.7 eV, respectively.

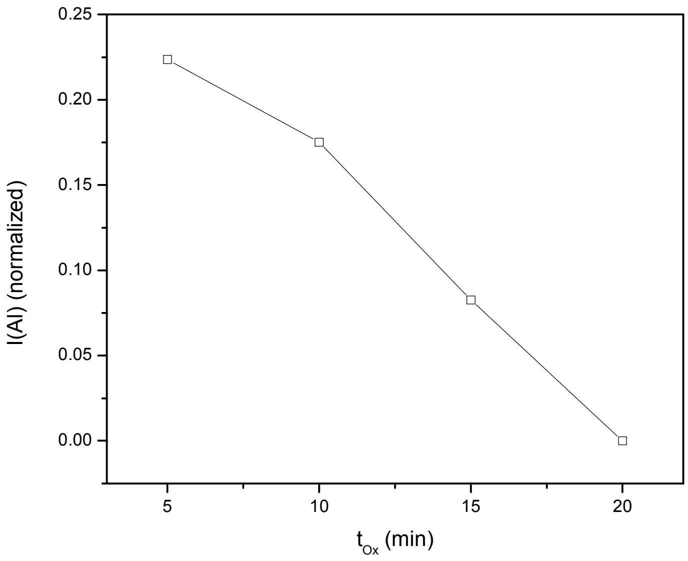

Fig. 5.24 The Al 2p core level intensity of a 1nm Al layer plotted versus the oxidation time.

A plot of the normalized intensity of the Al 2p core level as a function of the oxidation time is shown in Fig. 5.24. The intensities were obtained after making a Tougaard background subtraction and fitting three Gauss Lorentz sum peaks corresponding to Al_2O_{3+x}, Al_2O_3 and Al. It is observed from Fig. 5.24. that the rate of direct UV light assisted oxidation of the unoxidized Al follows a roughly Linear-to-Parabolic law. From Fig. 5.22 we concluded that for oxidation times greater than 20 min no change in the position and shape of the AlOx 2p core level peak is seen and this agrees well with the observation that the peak position and FWHM of the 20 min oxidized peak matches with that of sapphire.

In order to get an idea as to what is happening to the underlying Fe layer, we have observed the Fe 2p core level for the different oxidation times. It was observed that the underlying Fe shows no detectable traces of oxidation for oxidation times up to 20 min. Shown in Fig. 5.25 are the Fe 2p core levels of a Fe Ref film. It is observed that for a t_{Ox} greater than 20 min there is detectable evidence for the oxidation of the underlying Fe layer.

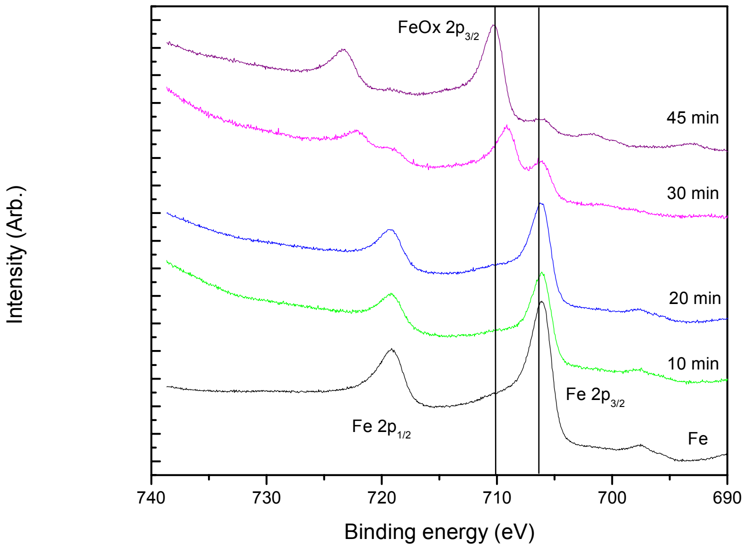

Fig. 5.25 The Fe 2p core level peaks showing detectable traces of oxidation for t_{Ox}= 25 min and beyond

5.2.1 Direct and indirect UV light assisted oxidation

In order to compare the rate of oxidation in the case of indirect and direct UV light assisted oxidation the XPS spectrum of two Al films oxidized directly and indirectly in UV light for 20 min were made. Shown below in Fig. 5.26 are the Al 2p core level spectra of such a 1 nm Al film oxidized for an oxidation time t_{Ox} = 20 min at a gas pressure of 133 mbar (100 Torr.) for the two cases

1. Direct UV light-assisted oxidation and

2. Indirect UV light-assisted oxidation.

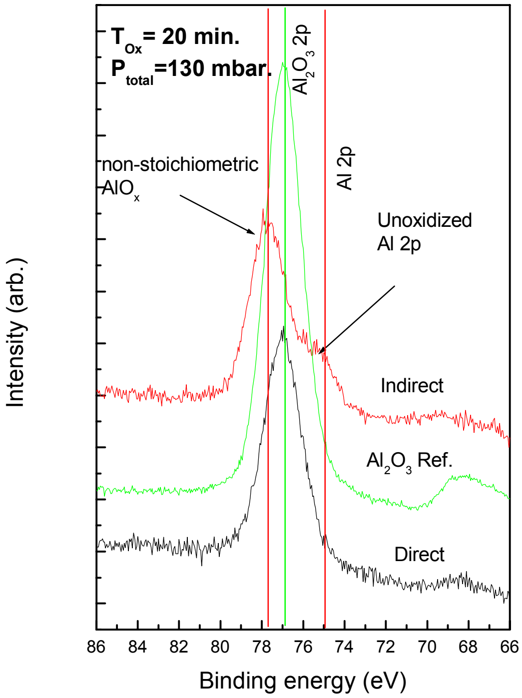

Fig. 5.26 Comparison of direct and indirect UV light assisted oxidation for t_{Ox}= 20 min. The spectra of indirect oxidized samples clearly shows the presence of unoxidized Al at a binding energy 74.5 eV. The peak of the direct oxidized Al layer coincides with the peak from sapphire.

Also shown is the Al 2p core level spectrum of a sapphire substrate, i.e. of Al 2p in Al_2O_3. It can be clearly seen that the spectra of the indirect oxidized film show traces of unoxidized or partially oxidized Al. Whereas the spectra of the direct UV light-assisted oxidized Al film coincides with that of the Al 2p core level in Al_2O_3, suggesting a nearly complete oxidation of the 1 nm Al layer.

5.2.2 Summary

The oxidation of the 1 nm Al film deposited on the epitaxial Fe(110)/Mo(110)/Sapphire substrate proceeds via the formation of a surface Al_2O_{3+x} layer as observed in the XPS spectrum of Al 2p core levels. The higher oxidation time of 20 min of the 1 nm Al film is not surprising considering the fact that it is grown on a very smooth epitaxial Fe(110) film. Thus there is clear evidence that the oxidation rate depends strongly on the film properties. A film with higher interstitial cations and defects oxidizes much faster.

A plot of the Al 2p core level intensity vs. the oxidation time follows a roughly linear-to-parabolic law which is unlike the case of the Al film deposited on a Co film. We attribute this to the different film characteristics and morphology.

A comparison of the direct and indirect UV light-assisted oxidation shows that direct UV light-assisted oxidation certainly accelerates the process of thin film oxidation.

5.3 Epitaxial tunnel junctions

In this section the results of the transport properties of epitaxial junctions are presented. The Fe(110)(20 nm)/MgO(111)(4 nm)/Fe(110)(15 nm)/Co(15 nm) epitaxial junctions were obtained by microstructuring the films grown on a sapphire (11-20) substrate with a Mo(110) buffer layer. A maximum *TMR* of 14% was observed at a temperature of 16 K as shown in Fig. 5.27 a), whereas the maximum *TMR* observed at 100 K is 7% Fig. 5.27

b) and the maximum *TMR* measured at room temperature with a very low bias voltage was 5%.

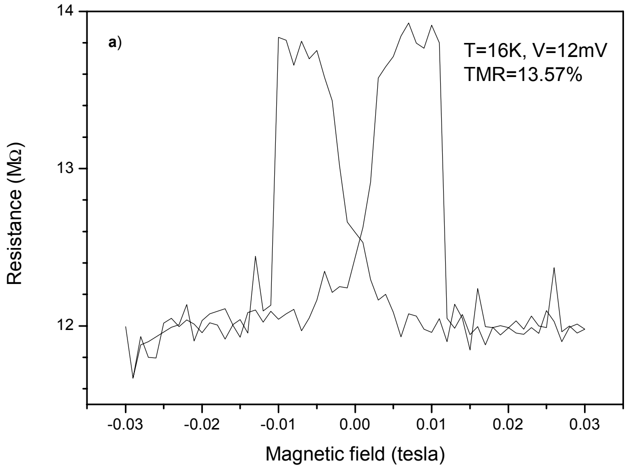

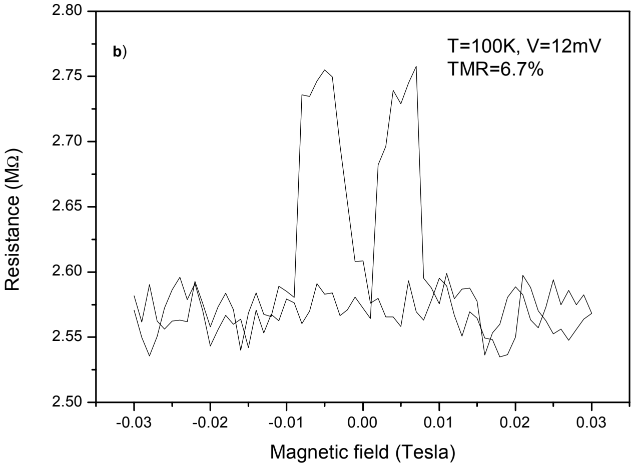

Fig. 5.27 The TMR curves at 16 K and 100 K of the epitaxial Fe(110)/MgO(111)(4 nm)/Fe(110) junction shown, respectively, in a) and b)

The Fe(110) orientation shows in spin-polarized angle resolved photoemission spectroscopy (SPARPES) measurements a spin polarization of about -80% of the electrons at the Fermi level [5.9] . It is therefore not clear as to why the TMR measurements of junctions with epitaxial Fe(110) electrodes show low TMR values. A possible reason for the same could be the formation of an iron oxide layer at the Fe(110)/ MgO(111) [5.10] interface or the loss of the spin polarization of the tunneling electrons within the MgO barrier layer. In order to understand the much lower *TMR*s measured and to get a deeper insight into the tunneling mechanism the temperature and bias dependence of the tunnel conductivity were studied.

As elaborated in chapter 3, the Glazmann Matveev (GM) model of inelastic tunneling via chains of localized defect states in the barrier was employed to analyze the temperature and bias dependence of the epitaxial tunnel junctions.

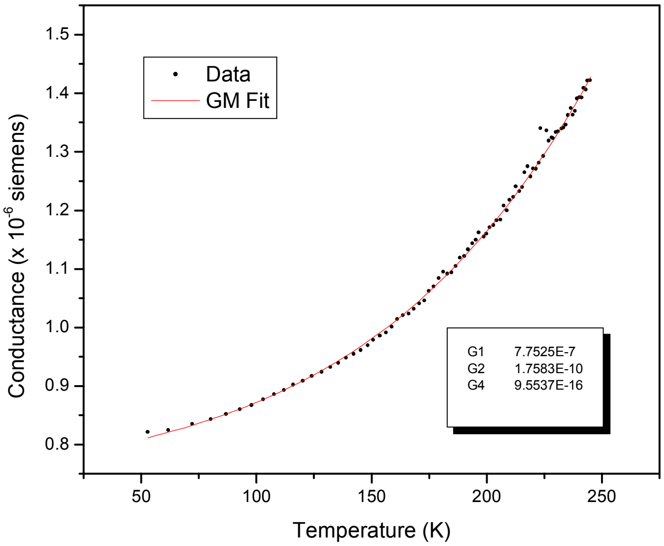

Fig. 5.28 Conductance versus Temperature plot of a Fe(110)(20 nm)/MgO(111)(4 nm)/ Fe(110)(15 nm)/Co(15 nm) junction exhibiting tunneling behavior. The line is a fit to the data according to the GM model of inelastic tunneling via localized defect states in the barrier with n = 1,2 and 4.

Shown in Fig. 5.28 is the measured conductance versus temperature plot of a Fe(110) /MgO(111)(4 nm)/Fe(110) junction, also shown is the GM fit with n = 1, 2 and 4.

The temperature dependence satisfies the Rowell criteria of insulator like Conductance vs. Temperature and the GM fit clearly demonstrates the $T^{4/3}$ dependence at low temperatures and $T^{18/5}$ dependence at higher temperatures. This corresponds to inelastic tunneling via chains of localized defect states in the barrier with n = 2 at low temperatures and n = 4 at higher temperatures. Since it is reasonable to assume that inelastic tunneling destroys the spin polarization of the tunneling electrons, it can be said that the absence or low values of the *TMR*s measured is due to the localized defect states within the MgO barrier. Fig. 5.29 shows the calculated normalized *TMR* vs. Temperature curve obtained by inserting the values of G_0, G_1, G_2 and G_4 (Fig. 5.28) into Eqn. 3.15.

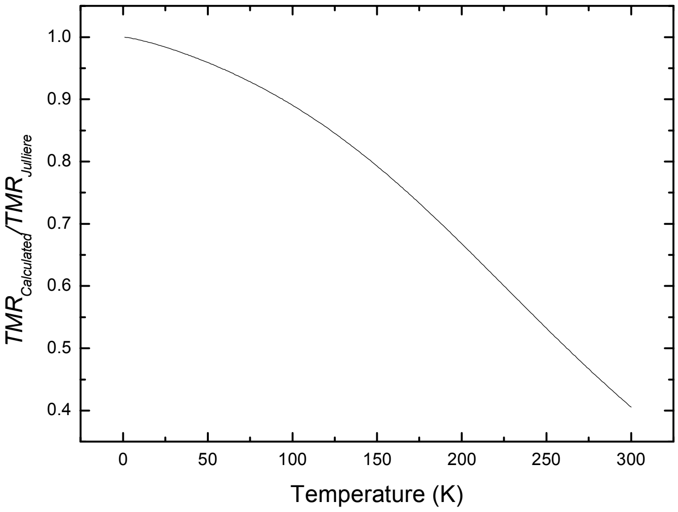

Fig. 5.29 The calculated normalized *TMR* vs. Temperature curve obtained by inserting the fit parameters G_0, G_1, G_2 and G_4 from Fig. 5.28 in Eqn. 3.15

The conductance versus temperature plot of a junction shown in Fig. 5.30 is an interesting example of the dominance of the tunnel conductivity by different chains at different temperatures. The tunnel conductivity below 35 K, as is evident from the constant value of the tunnel conductivity, is dominated by the direct (n=0) and indirect (n=1) elastic tunneling terms. The temperature dependence of the conductivity above 35 K exhibits a $T^{4/3}$ behavior typical of inelastic conductance via chains of two localized defect states, i.e. n=2.

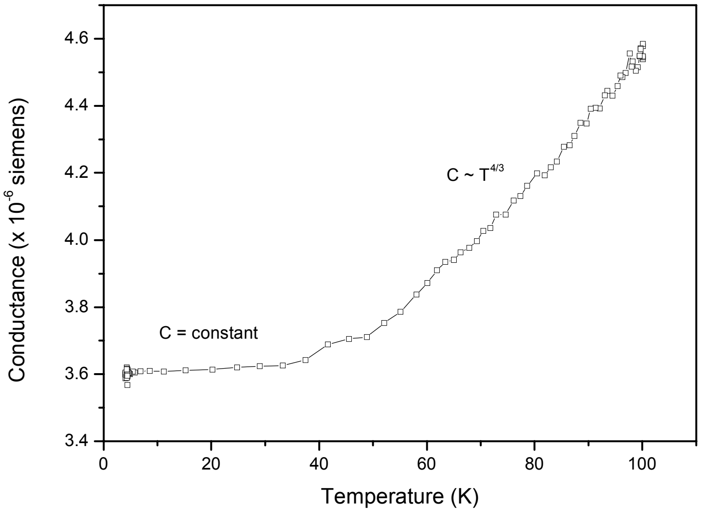

Fig. 5.30 The conductance versus temperature of a Fe(110)(20 nm)/MgO(111)(4 nm)/ Fe(110)(15 nm)/Co(15 nm) junction showing the cross over of the chains from n= 0 and 1 to the n= 2 at a temperature of about 35 K .

5.3.1 Bias dependence

The measured bias dependence of the tunnel conductance were also analyzed in terms of the GM model. Fig. 5.31 shows the conductance vs. bias voltage of a Fe(110)(20 nm)/ MgO(111)(4 nm)/Fe(110)(15 nm)/Co(15 nm) junction measured at a temperature of 150K. The bias dependence of the conductivity can be fitted by a sum of $T^{4/3}$, $T^{5/2}$ and $T^{18/5}$ dependence which in terms of the GM model corresponds to inelastic tunneling via chains of n = 2,3 and 4 defect states in the barrier. At low bias voltages the $T^{4/3}$ term dominates the conductivity. At intermediate bias voltage the $T^{5/2}$ term dominates the conductivity and at high bias voltages the $T^{18/5}$ term dominates the tunnel conductivity. A calculation of the elastic and inelastic components of the conductivity at a bias voltage of 0.85V shows that the inelastic component of the conductivity is 43 times the elastic component of the conductivity. Under these circumstances, it is very likely that the tunneling electrons totally lose their spin polarization.

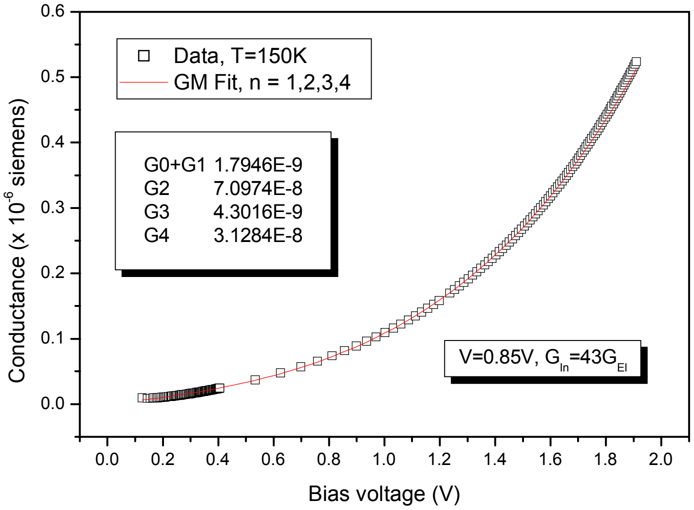

Fig. 5.31 The bias voltage dependence of the conductance of an epitaxial tunnel junction along with a GM fit. The inelastic component is 43 times the elastic component of the conductivity.

However, the same sample does show a finite *TMR* of 1.43% at a temperature of 150 K and a bias voltage of 0.85V. Therefore on calculating the possible elastic *TMR* one obtains a *TMR* of 63%, which corresponds to a calculated spin polarization of 68% for the Fe (110) film.

Again as in the previous sections the bias dependence of the *TMR* in magnetic tunnel junctions can also be understood and quantified with the help of the GM model by separating the elastic and the inelastic components of the tunnel conductivity.

Shown in Fig. 5.32 is the calculated normalized *TMR* as a function of the bias voltage. The *TMR* was calculated by fitting the bias voltage dependence of the conductance. In order to make a good fit the n = 2 and 3 terms have to be included.

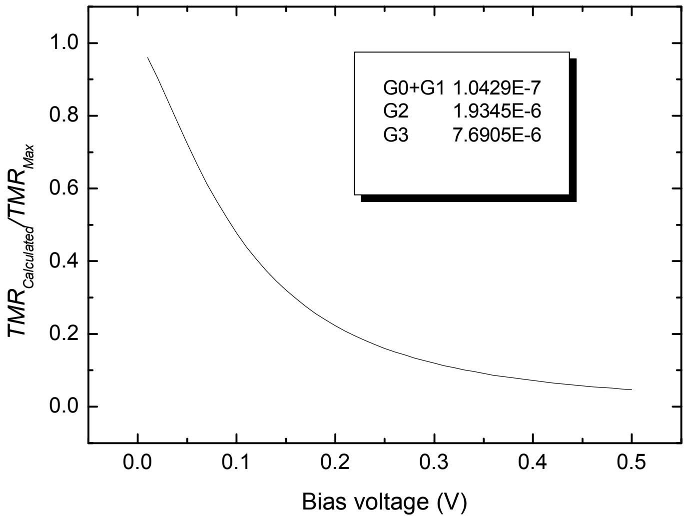

Fig. 5.32 The calculated normalized *TMR* vs. bias voltage curve obtained by inserting the GM fit parameters G_0, G_1, G_2 and G_3 in Eqn. 3.16

As a good example of the validity of GM model are the following *TMR*s of a junction measured at different bias voltages as shown in the following table.

Bias voltage (mV)	$TMR_{Inelastic}$ measured (%)	$G_{Inelastic}/G_{Elastic}$ GM Analysis	$TMR_{Elastic}$ calculated (%)
36	4.52	0.24	5.6
380	0.44	11.66	5.6

Table 5.3. The Bias voltage dependence of the observed $TMR_{Inelastic}$ ratio obtained from the GM model fit parameters at two different Bias voltages.

A Simmons fit to the bias voltage dependence of the tunnel current is also instructive. Fig. 5.33 shows a Simmons fit to the tunnel current as a function of the bias voltage. It is seen that the fit though not perfect is reasonably good. The barrier parameters obtained from the fit are d = 1.38 nm and ϕ = 3 eV. The reduced barrier thickness of 1.38 nm obtained from the Simmons fit is much smaller than the actual deposited 4 nm MgO barrier. The barrier height obtained from the Simmons fit varies from 0.4 eV to 3 eV. The reduced values of the barrier heights and thickness can be understood as follows: A Simmons fit to an imperfect barrier with defects would only calculate the effective barrier height and thickness of the barrier, which in the case of a barrier with defects would be smaller than the actual values.

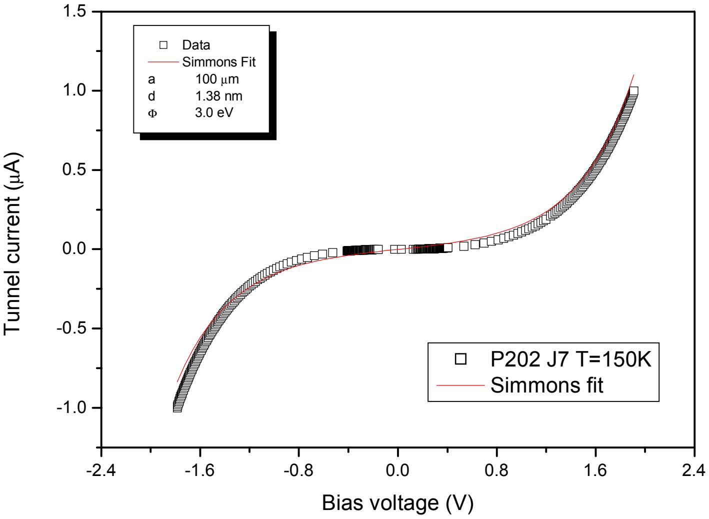

Fig. 5.33 A Simmons fit to the I-V characteristics of a Fe(110)(20nm)/MgO(111)(4 nm)/ Fe(110)(15 nm)/Co(15nm) tunnel junction yielding a barrier thickness 1.38 nm and a barrier height of 3 eV.

5.3.2 Summary

It is possible to obtain some insight into the loss of the *TMR*s by separating the elastic and inelastic component of the tunnel conductivity as suggested by the GM model. However, the inelastic component of the tunnel conductivity could not be the only mechanism responsible for the low TMR values observed for the following reasons:

1. GM model fits to most of the tunnel conductance versus bias voltage of the junctions together with the measured *TMR*s yield a $\mathrm{TMR}_{\mathrm{Elastic}}$ ratio of about 20% only at a temperature of 150 K.
2. The GM analysis of the junction showing the maximum *TMR* of 14% at 16 K gives $G_{\mathrm{Inelastic}} \ll G_{\mathrm{Elastic}}$. Therefore, it is for this particular junction not clear where the spin polarization of the tunneling electrons is lost. We assume that the

spin polarization is lost at the Fe(110)/MgO(111) interface due to the oxidation of the Fe layers [5.4, 5.10].

6 Conclusions

The Cabrera Mott theory of thin metal film oxidation could be employed to explain the oxidation of thin Al films with reasonable success. The different oxidation times of the 1 nm Al film on Co and Fe(110) indicate the importance of the film morphology in the oxidation of the Al films. Strangely, both the inverse logarithmic law of thin oxide film formation and the direct logarithmic law of thin oxide film formation could be used to fit the oxide thickness vs. oxidation time. The direct UV light-assisted oxidation certainly accelerates the rate of thin Al film oxidation.

TMR was observed in both Co/AlOx/Co tunnel junctions and epitaxial Fe(110)/MgO(111)/Fe(110) tunnel junctions. Clear differences with respect to *TMR* values and the temperature dependence of the tunnel conductance were noted in shadow mask deposited and microstructured junctions. The temperature and bias dependence of the tunnel conductivity and *TMR* of the TMR junctions could be fairly well understood in terms of the Glazman Matveev model of inelastic tunneling via defect states.

Thus both the Cabrera Mott theory and the Glazman Matveev model when applied to the oxide barriers employed in tunnel junctions stress the importance and role of the interstitials and defects in the oxide barriers.

References

References to Chapter 1

[1.1] M. N. Baibich, J. M. Broto, A. Fert, F. Nguyen Van Dau, F. Petroff, P. Eitenne, G. Creuzet, A. Friederich, and J. Chazelas, Phys. Rev. Lett. **61**, 2472 (1988).

[1.2] G. Binasch, P. Grünberg, F. Saurenbach, and W. Zinn, Phys. Rev. B **39**, 4828 (1989).

[1.3] W. Weber, D.A. Wesner, G. Güntherodt and U. Linke Phys. Rev. Lett. **66** (1991).

[1.4] B. N. Engel, 4th International Symposium on Metallic Multilayers, MML '01, p. 26, 2001.

[1.5] P. M. Tedrow and R. Meservey, Phys. Rev. Lett. **26,** 192(1971).

[1.6] P. M. Tedrow and R. Meservey, Phys. Rev. B **7**, 318 (1973).

[1.7] Julliere, Phys. Lett. **54A**, 225 (1975).

[1.8] S. Maekawa and U. Gäfvert, IEEE Trans. Magn. **18**, 707 (1982).

[1.9] Y. Suezawa, and Y. Gondo, in *Proceedings of the International Sypmposium on Physics of Magnetic Materials, Sendai* 1987 (World Scientific, Singapore 1987), p. 303.

[1.10] J. C. Slonczewski, Phys. Rev. B **39**, 6995 (1989).

[1.11] T. Miyazaki, T. Yaoi, and S. Ishio, J. Magn. Magn. Mater. **98**, L7 (1991).

[1.12] T. Miyazaki, T. Yaoi, and S. Ishio, J. Magn. Magn. Mater. **126**, 430 (1993).

[1.13] J. Nowak, and R. Rauluszkiewicz, J. Magn. Magn. Mater. **109**, 79 (1992).

[1.14] R. Nakatani, and M. Kitada, J. Mater. Sci. Lett. **10**, 827 (1991).

[1.15] Y. Suezawa, F. Takahashi, and Y. Gondo, Jpn. J. Appl. Phys. **31**, L 1451 (1992).

[1.16] P. LeClair, J. S. Moodera, and R. Meservey, J. Appl. Phys. **76**, 6546 (1994).

[1.17] T. Miyazaki, and N. Tezuka, J. Magn. Magn. Mater. **139**, L231 (1995).

[1.18] J. S. Moodera, L. R. Kinder, T. M. Wong, and R. Meservey, Phys. Rev. Lett. **74**, 3273 (1995).

[1.19] P. Rottländer, H. Kohlstedt, H. A. M. De Gronckel, E. Girgis, J. Schelten, and P. Grünberg, J. Magn. Magn. Mater. **210**, 251 (2000).

[1.20] P. Rottländer, H. Kohlstedt, P. Grünberg and E. Girgis, J. Appl. Phys. **87**, 6067 (2000).

[1.21] A. Sommerfeld and H. Bethe, Handbuch der Physik von Geiger und Scheel (Julius Springer-Verlag, Berlin 1933), Vol. 24/2, p. 450.

[1.22] J. C. Fisher and I. Giaever, J. Appl. Phys. **32,** 172 (1961).

[1.23] J. G. Simmons, J. Appl. Phys. **34,** 1793 (1963).

[1.24] L. Neel, C. R. Acad. Sci. **255**, 1676 (1962).

[1.25] S, Tegen, I. Mönch, J. Schumann, H. Vinzelberg, and C. M. Schneider, J. Appl. Phys. **89,** 8169 (2001).

[1.26] P. LeClair, H. J. M. Swagten, J. T. Kohlhepp, R. J. M. van de Veerdonk, and W. J. M. de Jonge, Phys. Rev. Lett. **84**, 2933 (2000).

[1.27] U. May, K. Samm, H. Kittur, J.O. Hauch, R. Calarco, U. Rüdiger, G. Güntherodt, Appl. Phys. Lett. **78**, 2026-2028 (2001).

References to Chapter 2

[2.1] N. F. Mott Trans. Faraday Soc. **39**, 472 (1940)

[2.2] N. F. Mott Trans. Faraday Soc. **43**, 429 (1947)

[2.3] N. Cabrera and N. F. Mott, Rep. Prog. Phys. **12,** 163 (1949).

[2.4] A. T. Fromholdt, Jr: Theory of metal oxidation Vol. I, (North-Holland Publishing Company, Amsterdam 1976) p. 7.

[2.5] J. Bardeen, W. H. Brattian, and W. Shockley, J. Chem. Phys. **14,** 714 (1946).

[2.6] H. Okabe: Photochemistry of small molecules (John Wiley & Sons, New York 1978) p. 129.

[2.7] D. L. Blaluch, R. A. Cox, R. F. Hampson, J. A. Herr, J. Tore, and R. T. Watson, Phys. Chem. Ref. Data. **9**, 295 (1980).

[2.8] N. Cabrera, J. Terrien, and J. Hamon, Comptes Rendus **224,** 1558 (1947).

[2.9] N. Cabrera, Phil. Mag. **40**, 175 (1949A).

References to Chapter 3

[3.1] Sommerfeld and H. Bethe, *Handbüch der Physik von Geiger und Scheel* (Julius Springer-Verlag, Berlin, 1933), Vol. 24/2, p. 450.

[3.2] R. Holm, J. Appl. Phys. **22**, 569, 1951.

[3.3] J. G. Simmons, J. Appl. Phys. **34**, 1793, 1963.

[3.4] J. G. Simmons, J. Appl. Phys. **35**, 2655, 1964.

[3.5] W. F. Brinkman, R. C. Dynes, and J. M. Rowell, J. Appl. Phys. **41**, 1915, 1970.

[3.6] J. M. Rowell, *Tunneling phenomena in Solids*, Eds. E. Burstein and S. Lundqvist, Plenum press, 1969, p. 279.

[3.7] B. J. Jönsson-Akerman, R. Escudero, C. Leighton, S. Kim, I. K. Schuller, D. A. Rabson, Appl. Phys. Lett. **77**, 1870 (2000).

[3.8] D. A. Rabson, B. J. Jönsson-Akerman, A. H. Romero, R. Escudero, C. Leighton, S. Kim, I. K. Schuller, J. Appl. Phys. **89**, 2786 (2001).

[3.9] J. Halbritter, J. Appl. Phys. **58**, 1320, 1985.

[3.10] J. Halbritter, IEEE Trans. Magn. **MAG-19**, 799, 1983.

[3.11] J. Halbritter, IEEE Trans. Magn. **MAG-21**, 858, 1985.

[3.12] L. I. Glazman and K. A. Matveev, Sov. Phys. JETP **67**, 1266, 1988.

[3.13] Yizi Xu, D. Ephron and M. R. Beasley, Phys. Rev. B. **52**, 2843, 1995.

[3.14] Chang He Shang, J. Nowak, R. Jansen and J. S. Moodera, Phys. Rev. B **58**, R2917, 1998.

[3.15] Höfener, J. B. Philipp, J. Klein, L. Alff, A. Marx, B. Büchner and R. Gross, Europhys. Lett. **50**, 681, 2000.

References to Chapter 4

[4.1] H. Okabe, Photochemistry of small molecules, John Wiley & Sons, New York, p. 129.

[4.2] T. Miyazaki, and N. Tezuka, J. Magn. Magn. Mater. **139**, L231 (1995).

[4.3] P. Rottländer, H. Kohlstedt, P. Grünberg and F. Girgis, J. Appl. Phys, **87**, 6067 (2000).

[4.4] H. Hertz, Ann. Physik **31**, 983 (1887).

[4.5] A. Einstein, Ann. Physik **17**, 132 (1905).

[4.6] C. D. Wagner, W. M. Riggs, L. E. Davis, J. F. Moulder, G. E. Muilenberg, Handbook of X-ray Photoelectron Spectroscopy, Perkin-Elmer Corporation.

[4.7] S. Hüfner, Photoelectron Spectroscopy, 2nd Edition, Springer-Verlag.

[4.8] D. A. Shirley, Phys. Rev. B **5**, 4709 (1972).

[4.9] S. Tougaard, J. Vac. Sci. Technol. A **5**, 1230 (1987).

[4.10] M. Fonin, Yu. S. Dedkov, J. Mayer, U. Rüdiger, and G. Güntherodt, Phys. Rev. B **68**, 45414 (2003).

References to Chapter 5

[5.1] S. Tougaard, J. Vac. Sci. Technol. **A5(4)**, 1230 (1987).

[5.2] J. Nogues and I. K. Schuller, J. Magn. Magn. Mater. **192**, 203 (1999).

[5.3] I. I. Oleinik, E. Yu. Tsymbal, and D. G. Pettifor, Phys. Rev. B. **62**, 3952 (2000).

[5.4] X. –G. Zhang, W. H. Butler, and A. Bandyopadhyay, Phys. Rev. B **68**, 092402 (2003).

[5.5] I. Giaever in *Tunneling Phenomena in Solids*, Eds. Burstein & Lundqvist, Plenum Press, New York 1969, p. 27.

[5.6] D. D. Eley nd P. R. Wilkinson, Proc. R. Soc. London, **Ser A 254**, 327 (1960).

[5.7] N. F. Mott, Trans. Faraday Soc. 35, 1175 (1939).

[5.8] N. F. Mott, Trans. Faraday Soc. 36, 1 (1940).

[5.9] Yu. Dedkov, Ph. D. Thesis, Spin-resolved photoelectron spectroscopy of oxidic half-metallic ferromagnets and oxide/ ferromagnet interfaces, RWTH Aachen, 2004.

[5.10] Yu. S. Dedkov, M. Fonin, G. Güntherodt, and U Rüdiger, to appear in Appl. Phys. Lett.

List of publications

Parts of this work have been previously published or communicated:

U. May, “Magnetische Schichten für den Einsatz in der Magnetoelektronic”, Dissertation RWTH-Aachen, 2001

J.O. Hauch, M. Fonine, U. May, R. Calarco, H. Kittur, J.M. Choi, U. Rüdiger, G. Güntherodt: “The Growth of Transition Metals on H-Passivated Si(111) Substrates”, Adv. Funct. Mater. 11, 179-185 (2001)

U. May, R. Calarco, J.O. Hauch, H. Kittur, M. Fonine, U. Rüdiger, G. Güntherodt: “Characterization of epitaxial growth of Fe(110) on (11-20) sapphire substrates driven by Mo(110) seed layers”, Surf. Sci. 489, 144-150 (2001)

U. May, K. Samm, H. Kittur, J.O. Hauch, R. Calarco, U. Rüdiger, G. Güntherodt: “Temperature-dependent Magnetoresistance of Magnetic Tunnel Junctions with UV Light-Assisted Oxidized Barriers”, Appl. Phys. Lett. **78**, 2026-2028 (2001)

U. Rüdiger, R. Calarco, U. May, K. Samm, J.O. Hauch, H. Kittur, M. Sperlich, G. Güntherodt: “Temperature Dependent Resistance of Magnetic Tunnel Junctions as a Quality Proof of the Insulating Barrier”, J. Appl. Phys. **89**, 7573-7575 (2001)

Conference Participations:

H. Kittur, U Rüdiger, U. May, R. Calarco, K. Samm, J. Hauch, G. Güntherodt and G. Rangarajan: "Tunneling MR in Magnetic Multilayers and their High Potential Applications as Magnetoresistive Sensors and RAM's", Advances in Magnetic Materials and Applications, Magnetics Society of India, Chennai, 2000

H. Kittur, U Rüdiger, U. May, R. Calarco, J. Hauch, K. Samm, R. Ghadimi, K. Brüggemann and G. Güntherodt: "Temperature and bias dependence of resistance and magnetoresistance of magnetic tunnel junctions", International Symposium on Advances in Superconductivity and Magnetism: Materials, Mechanisms and Devices, Tata Institute of Fundamental Research, Mumbai and Mangalore University, Mangalore, 2001

H. Kittur, U Rüdiger, U. May, R. Calarco, J. Hauch and G. Güntherodt: "Epitaxial growth of bcc Fe(110) on sapphire(11-20) substrates driven by a Mo(110) seed layer", International Symposium on Advances in Superconductivity and Magnetism: Materials, Mechanisms and Devices, Tata Institute of Fundamental Research, Mumbai and Mangalore University, Mangalore, 2001

R. Calarco, H. Kittur, J. Hauch, K. Samm, U. May, R. Ghadimi, U Rüdiger and G. Güntherodt: "Co/AlOx/Co/Si(100) Magnetic tunnel junctions with UV-light assisted oxidized barriers", 4th International Symposium on Metallic Multilayers, Aachen, Germany, 2001

Acknowledgements

I would like to take this opportunity to acknowledge the help of many people who have made this work possible and thank them for their help and support.

First and foremost, I would like to thank Prof. Dr. G. Güntherodt, for giving me the opportunity to perceive research in the frontier fields of Physics. I thank him for his constant support and encouragement throughout the period of my research. His guidance was of great value. Above all, I thank him for having borne with patience many of the mistakes made by me in the course of my work at the 2nd Physics Institute, Aachen.

I thank our former group leader and mentor Prof. Dr. Ulrich Rüdiger, for the constant guidance, suggestions and comments during the tenure of my work. I also thank him for co-refereeing this work.

Special thanks to my former colleague and guide Dr. U. May for having trained me in UHV techniques and for having patiently answered many of my queries. Many thanks to my colleague J. O. Hauch for all his help and the great time we had in the MBE lab. Without his co-operation research work in the MBE lab would have been impossible. I also thank him for the crucial study material provided by him. My thanks go out to our former Post-Doc Dr. R. Calarco for her guidance and friendliness in the laboratory. I owe many thanks to R. Ghadimi for all his help and suggestions. Many thanks to M. Fraune

for the tedious and time consuming work of microstructuring the junctions. This work would not have been possible without the help and contributions of these people.

I thank my former colleague in the transport measurement laboratory, K Samm for all her help and co-operation. Special thanks to K. Brüggemann for all the Lab-View programming work carried out in the transport measurement laboratory and for his help, cooperation and friendliness.

Many thanks to Dr. B. Beschoten and Dr. G. Richter, who inspite of their busy schedules offered help in handling and rescuing the Cryostat in the transport measurement laboratory.

I thank all my colleagues, C. König, M. Fonine, M. Sperlich, Y. Dedkov, A. Tillmanns, J. Keller, I. Dostenko, M. Heidkamp, K. Y. Choi, D. Heydhausen and many others for the help and co-operation. I also thank our Post-Doc Dr. Christian Papusoi for the friendly atmosphere he helped in creating in the MBE lab.

I express my heartfelt thanks and gratitude to the techinal staff Mr. Petersen, Mr. Klaus, Mr. Dieter, Mr. Roeger and Mr. Geulen. I also express my heartfelt thanks and gratitude for the workshop staff, especially Mr. Kordt, Mr. Retetzki, Robert and Franz. All the scientific work would not have been possible without their help and work in innumerable instances.

No amount of thanks would be sufficient for the pleasant guten Morgens and many other good wishes and help from the secretarial staff of Miss. Schüren and Miss Weinkauf. I give them many thanks.

I especially thank my friend from the 1st Physics Institute Dr. S. Selvaraj for the many XRR measurements made for the purpose of calibration.

I thank all my friends and colleagues who have either directly or indirectly contributed and helped in some way or the other.

I once again take this opportunity to heart fully thank my family and especially my parents for their love, patience, support, co-operation and guidance.

Finally special thanks and acknowledgements to my wife Pooja without whose love, patience, support, co-operation, guidance and help this work would not have been possible.

Noch mal, vielen Dank alle zusammen!

Curriculum Vitae

Name : **Harish Kittur**

Sex : Male

Date of birth : 29. April 1973

Place of birth : Gadag

Nationality : Indian

-1989 : Secondary School Certificate, St. Michael’s High School, Mumbai

1989-1991 : Higher Secondary Certificate, Kirti M. Dongursee College, Mumbai

1991-1994 : Bachelor of Science, P.C.Jabin College,Karnataka University,Dharwad

1994-1996 : Master of Science(Physics), Indian Institute of Technology, Bombay

1997-1999 : Master of Technology, Indian Institute of Technology, Madras

Since 1999 : Scientific assistant at the 2nd Physics Institute, RWTH, Aachen

02.07.2004 : Doktorprüfung (Ph.D. Examination)